University of Stuttgart
Germany

Bachelor Thesis

Phase stability of an optical superlattice setup for ultracold dysprosium atoms

Paul Michael Uerlings

March 1, 2019

examiner:
Prof. Dr. Tilman Pfau

University of Stuttgart
5. Physikalisches Institut
Pfaffenwaldring 57, DE-70569 Stuttgart

Zusammenfassung

Im Rahmen dieser Arbeit wird die Phasenstabilität eines optischen Übergitters untersucht. Das optische Übergitter ist ein wichtiger Bestandteil eines Quantengas-Mikroskops und Teil des neuen Dysprosium Experiments der „Dipolar Quantum Gases“ Gruppe des 5. Physikalischen Instituts der Universität Stuttgart. Ultrakalte Atome, welche in optischen Gittern eingefangen werden, eignen sich nicht nur um Experimente der Atomphysik durchzuführen. Mit optischen Gittern können zum Beispiel die Kristallstrukturen von Festkörpern modelliert werden [1]. Dies ermöglicht es Festkörper mit einzelnen Atomen zu modellieren und die Theorien und Modelle der Festkörperphysik zu testen [2, 3]. Ein optisches Übergitter entsteht, wenn sich zwei optische Gitter mit unterschiedlichem Gitterabstand überlagern. Mit solchen Systemen ist es möglich komplexere Strukturen mit großer Variabilität zu erzeugen. Indem man die relative Phase der einzelnen Gitter zueinander verändert, ist es möglich die Form des Übergitters zu variieren. Diese Variabilität führt allerdings auch dazu, dass das optische Übergitter sensitiv gegenüber äußeren Einflüssen, ist welche die relative Phase beeinflussen können. Um die Verlässlichkeit und die Reproduzierbarkeit des Experiments zu gewährleisten, ist es notwendig, dass das optische Übergitter phasenstabil gegenüber solchen Einflüssen ist.

Die Experimente, welche in dieser Arbiet durchgeführt wurden, zeigten, dass sich die relative Phase, selbst unter optimalen Bedingungen, durch Umgebungseinflüsse wie Temperatur und Druckänderungen auf einer Skala von $0{,}05\,\pi$ pro Stunde verändert. Die Änderung der relativen Phase auf kleineren Zeitskalen, durch zum Beispiel lokale Veränderungen des Luftdrucks, ist in der Größenordnung von $0{,}005\,\pi$. Veränderungen dieser Größenordnung sind zu groß, um verlässliche und reproduzierbare Experimente durchzuführen. Die langzeit Stabilität kann durch regelmäßigen Kalibrierungsmessungen verbessert werden [4] jedoch bedarf es einer aktiven oder passiven Stabilisierung der relativen Phase auf kleineren Zeitskalen. Im Rahmen dieser Arbeit wurde außerdem gezeigt, dass eine aktive Stabilisierung der relativen Phase mit Hilfe einer Piezo-angetriebenen Positionierungssystems möglich ist.

Abstract

This thesis reports on the first experimental tests regarding the phase stability of a optical superlattice setup which will be part of a new quantum gas microscope with atomic Dysprosium. The optical superlattice will be used to probe and manipulate a dipolar quantum gas with single-site resolution. The superlattice will be created by superimposing a lattice with a short spatial periodicity, created by interfering light at 362 nm and a lattice with a double the spatial periodicity, using light with a wavelength of 724 nm. The relative phase between the two lattices determines the shape of the potential. This allows for the creation of double well potentials with arbitrary energy shifts and potential barriers between the two wells. This high degree of control of the potential shape also makes the superlattice very susceptible to shifts in its relative phase. Such small shifts can arise from the fluctuations in refractive index due to changing environmental conditions. It was discovered that, under optimal conditions with negligible thermal expansion, these shifts are expected to be on the order of $0.05\,\pi$ per hour. On smaller time scales the shifts can still be on the order of up to $0.005\,\pi$ due to local changes, for example in air pressure caused by air flow. Changes in the relative phase on these scales would make reliable and repeatable experiments challenging. Therefore the modified Edlén equation, as a means of calculating the refractive index, can be used to predict the resulting phase change. During this thesis the validity of the modified Edlén eqn. was confirmed but also limitations could be demonstrated.

Furthermore a piezo-actuated positioning stage was used to actively change the relative phase. This is a first step towards active phase stabilization of the superlattice setup.

Ehrenwörtliche Erklärung

Gemäß der Prüfungsordnung der Universität Stuttgart für den Bachelorstudiengang Physik vom 31. Juli 2015 versichere ich,

1. dass ich diese Arbeit selbst verfasst habe,
2. dass ich keine anderen als die angegebenen Quellen benutzt und alle wörtlich oder sinngemäß aus anderen Werken übernommenen Aussagen als solche gekennzeichnet habe.
3. dass die eingereichte Arbeit weder vollständig noch in wesentlichen Teilen Gegenstand eines anderen Prüfungsverfahrens gewesen ist, und
4. dass das elektronische Exemplar mit den anderen Exemplaren übereinstimmt.

Stuttgart, 01.03.2019	*Paul Uerlings*
Ort, Datum	Unterschrift

Contents

1. Introduction

Since the invention of the LASER [1] in the 1960s [5], many new experimental techniques such as high resolution laser spectroscopy have opened up new fields of atomic physics [6]. Techniques such as laser cooling and trapping of atoms allowed for more precise measurements of their internal structure. These advances also started a quest to confirm Bose and Einstein's theory of a Bose-Einstein condensate (BEC), a new form of matter proposed by Einstein in 1924 [7]. The first BEC was produced in June 1995 by E. CORNELL and C. WIEMAN at the University of Colorado at Boulder with a gas of Rubidium atoms cooled to near absolute zero temperature[8]. Since then, many more atomic species were successfully condensed into a BEC. In 2005 PFAU et. al produced the first BEC using magnetic Chromium atoms [9] featuring a long-range and anisotropic magnetic dipole-dipole interaction [10] in addition to the normal contact interactions. This opened up the field of studying dipolar phenomena using ultracold quantum gases. The Dipolar Quantum Gases group at the 5th institute of physics at the University of Stuttgart has since replaced Chromium atoms with Dysprosium. Dysprosium has the highest magnetic moment in the periodic table thus enabling many new discoveries like the observation of quantum droplets [11, 12] and the anisotropic superfluid behavior of dipolar quantum gases [13]. Recently transient supersolid properties were observed in an array of dipolar quantum droplets [14, 15].
In the new dipolar quantum gas experiment that is currently being build an optical superlattice will be implemented in the experiment as a part of a quantum gas microscope. At the time of writing this thesis only a few quantum gas microscopes exist. As far as we know only one other dipolar quantum gas microscope is currently being built [16]. Ultracold atoms in optical lattices are not only of interest in studying atomic physics but also for solid-state quantum simulations. They are a proven tool for modeling quantum many-body systems. Optical lattices can for example be used to model crystalline structures such as those found in complex solid-state systems with very high degrees of control [1]. Atoms trapped in optical lattices are also ideal for simulating the Hubbard-Model, a model used in solid-state physics to describe the interactions between electrons in a lattice. One breakthrough with the Hubbard-Model was the observation of the superfluid to Mott insulator phase transition [3, 2] whereby increasing the lattice depth the initial superfluid quantum gas lost its superfluid characteristics.
By shifting the relative phase between the two lattices the resulting potential can be changed. These systems offer the possibility to create more complex or disordered systems with high degrees of control [17]. By combining the important discoveries that have been made by studying ultracold atoms in optical lattices with the single-site imaging capability of a quantum gas microscope, the new ultracold dysprosium experiment with its dipolar quantum gas microscope will give rise to a wide range of novel experiments.
An optical superlattice is generated by superimposing two independent optical lattices with different lattice spacing. The optical superlattice setup will provide a high degree of variability over the potential shape that the atoms will be trapped in. However the optical

[1] **L**ight **a**mplification **b**y **s**timulated **e**mission **o**f **r**adiation

superlattice is also very susceptible to environmental changes. Small shifts in the relative phase between the two individual lattices, due to the dispersion of air, can significantly change the shape of the superlattice potential [18]. Within this thesis, the phase stability of the planned superlattice setup is tested in order to develop an understanding of the experimental requirements for a stable optical superlattice setup. Also the validity of the modified Edlén equation as a means of predicting the phase change by calculating the change of the refractive index of air is tested.

2. Interferometry

The wave-like characteristics of light lead to many interesting phenomena. Electromagnetic waves, like other waves, can be superimposed causing interference. In general this interference takes place on a timescale too fast to be observed because the two interfering waves are not coherent. Only if the electromagnetic waves are temporal and/or spacial coherent can this superposition create stationary interference fringes that can be observed. A spatially periodic interference pattern, also called an optical lattice, is created as a result of multiple coherent waves interfering with each other. The properties of the planned superlattice, like the lattice geometry or a sufficient stability, can only really be measured with atoms that are trapped inside it.
However, in order to develop an understanding about the stability of the proposed setup an one-dimensional optical superlattice is generated using a Michelson interferometer setup. With this setup spatially periodic interference patterns resembling optical lattices can be realized. The stability of these pattern, like that of the optical superlattice, is characterized by the phase between the waves generating them. In the following sections theory behind the interference of multiple coherent plane waves is discussed in order to be able to characterize the influence of external parameters like temperature, pressure and humidity on the stability of the planned superlattice.

2.1. Wave optics

In vacuum ($n_{\text{vac}} = 1$) and without any external materials that can generate currents ($\mathbf{j} = 0$) and charge densities ($\rho = 0$) the *Maxwell equations* read as follows:

$$\nabla \cdot \mathbf{E} = 0 \qquad \nabla \cdot \mathbf{H} = 0 \qquad \nabla \times \mathbf{E} = -\mu_0 \frac{\partial}{\partial t}\mathbf{H} \qquad \nabla \times \mathbf{H} = \epsilon_0 \frac{\partial}{\partial t}\mathbf{E} \tag{2.1}$$

Using the vector identity $\nabla \times (\nabla \times \mathbf{E}) = \nabla(\nabla \cdot \mathbf{E}) - \nabla^2 \mathbf{E}$ and the *Maxwell equations* (2.1), electromagnetic waves propagating through a vacuum can be described by a second-order partial differential equation, also called the wave equation:

$$\left(\nabla^2 - \frac{1}{c^2}\frac{\partial^2}{\partial t^2}\right)\mathbf{E}(\mathbf{r}, t) = 0 \tag{2.2}$$

In the simplest case of monochromatic harmonic waves, separation of variables lead to [2]

$$\mathbf{E}(\mathbf{r}, t) = \Re e\{\mathbf{E}(\mathbf{r})e^{-i\omega t}\}\,. \tag{2.3}$$

With this ansatz and the dispersion relation $\omega^2 = c^2\mathbf{k}^2$, the wave equation (2.2) can be transformed into the *Helmholtz equation*

$$\left(\nabla^2 + \mathbf{k}^2\right)\mathbf{E}(\mathbf{r}) = 0 \tag{2.4}$$

which only depends on the position $\mathbf{r}$ [19].

[2] using the real part limits the solution to positive frequencies

2.2. Interference of two plane waves

Plane waves are the characteristic solution of the *Helmholtz equation* (2.4) when using the cartesian nabla operator $\left(\nabla = (\frac{\partial}{\partial x}, \frac{\partial}{\partial y}, \frac{\partial}{\partial z})\right)$. A plane wave emitted by a coherent light source can be written as:

$$\mathbf{E}(\mathbf{r}) = E_0 \cdot \cos\left(\omega t - \mathbf{k} \cdot \mathbf{r}\right) \tag{2.5}$$

When detecting electromagnetic waves the electric field can not directly be observed an rather the intensity I which is defined as

$$I \propto \mathbf{E}^2 \tag{2.6}$$

is measured. When superimposing two plane waves with the same polarization, consequently their electric fields add up resulting in:

$$I \propto \left(E_1(\mathbf{r}_1) + E_2(\mathbf{r}_2)\right)^2 \tag{2.7}$$

Inserting two plane waves with the same amplitude E_0 into eq. (2.7) yields:

$$I \propto E_0^2 \cdot \left[\cos\left(\omega_1 t - \mathbf{k_1} \cdot \mathbf{r_1}\right) + \cos\left(\omega_2 t - \mathbf{k_2} \cdot \mathbf{r_2}\right)\right]^2 \tag{2.8}$$

In the case where both plane waves have the same frequency and $\varphi_i = \mathbf{k_i} \cdot \mathbf{r_i}$ the equations reads:

$$\begin{aligned} I \propto E_0^2 \cdot &[\cos^2\left(\omega t - \varphi_1(\mathbf{r}_1)\right) + \cos^2\left(\omega t - \varphi_2(\mathbf{r}_2)\right) \\ &+ 2\cos^2\left(\omega t\right)\cos\left(\varphi_1(\mathbf{r}_1)\right)\cos\left(\varphi_2(\mathbf{r}_2)\right) \\ &+ 2\sin^2\left(\omega t\right)\sin\left(\varphi_1(\mathbf{r}_1)\right)\sin\left(\varphi_2(\mathbf{r}_2)\right) \\ &+ 2\sin(\omega t)\cos(\omega t)[\cos(\varphi_1(\mathbf{r}_1))\sin(\varphi_2(\mathbf{r}_2)) + \sin(\varphi_1(\mathbf{r}_1))\cos(\varphi_2(\mathbf{r}_2))]] \end{aligned} \tag{2.9}$$

Because of the very fast oscillation of electromagnetic field [3] the detector time-averages over many periods of the electromagnetic wave. Time averaging of equation (2.9) gives $< \cos^2(\omega t) >_t = 1/2$ and $< \sin(\omega t)\cos(\omega t) >_t = 0$ thus yielding the time-averaged intensity $\bar{I}$[20].

$$\bar{I} \propto E_0^2 \cdot [1 + \cos(\Delta\varphi(\mathbf{r}_1, \mathbf{r}_2))] \tag{2.10}$$

Where the phase difference between the two plane waves is defined as

$$\Delta\varphi(\mathbf{r}_1, \mathbf{r}_2) \equiv \varphi_1(\mathbf{r}_1) - \varphi_2(\mathbf{r}_2)\,. \tag{2.11}$$

This equation shows that the intensity $\bar{I}$ can vary between 0 and $2E_0^2$ depending on the phase difference $\Delta\varphi$. Because the cosine function has a periodicity of 2π and $\bar{I}(\phi(\mathbf{r})) = \bar{I}(\phi(\mathbf{r}) + 2\pi)$, a repeating interference pattern is observed.

[3] for visible light these oscillations take place on a pico- or femto-second timescale [19]

Two plane waves propagating in the same direction: If both waves propagate in the same direction, their wave vectors $\mathbf{k}$ are equal. The phase difference can then be expressed as a function of path difference using $k = 2\pi/\lambda$:

$$\begin{aligned}\Delta\varphi(\mathbf{r}_1, \mathbf{r}_2) &= \frac{2\pi}{\lambda}\left(|\mathbf{r}_1 - \mathbf{r}_2|\right) \text{ or} \\ \Delta\varphi(\mathbf{r}_1, \mathbf{r}_2) &= \frac{2\pi}{\lambda_0} \cdot n\left(|\mathbf{r}_1 - \mathbf{r}_2|\right) = \frac{2\pi}{\lambda_0} \cdot \Lambda\end{aligned} \tag{2.12}$$

Where $n = \lambda_0/\lambda$ is the refractive index of the medium the light is traveling trough.
The optical path difference (OPD) is defined as $\Lambda = n\left(|\mathbf{r}_1 - \mathbf{r}_2|\right)$ [21].
In the case of an Michelson interferometer this means that the intensity on the plane of detection stays constant and that a change in the OPD changes the intensity on the whole plane. In practice this cannot be easily observed because common light sources emit diverging beams of light. This divergence leads to different angles of tilt and the formation of alternating light and dark rings [20]. These kind of interference fringes are depicted in fig. 2.1 (a).

General case: In the general case, both waves do not propagate in exactly the same direction and thus do not have the same wave vectors. In the case of the Michelson interferometer this can be achieved by tilting one of the mirrors. In the following let us suppose that we tilted one mirror by an angle of $\alpha/2$ around the z-axis. As a result the reflected wave will have a tilt of α with respect to the y-axis. In this case the two wave vectors are:

$$\mathbf{k}_1 = \frac{2\pi}{\lambda}\begin{pmatrix}\sin(\alpha)\\ \cos(\alpha)\\ 0\end{pmatrix} \quad \text{and} \quad \mathbf{k}_2 = \frac{2\pi}{\lambda}\begin{pmatrix}0\\ 1\\ 0\end{pmatrix} \tag{2.13}$$

With the two position vectors:

$$\mathbf{r}_1 = \begin{pmatrix}x_d\\ r_1\\ z_d\end{pmatrix} \quad \text{and} \quad \mathbf{r}_2 = \begin{pmatrix}x_d\\ r_2\\ z_d\end{pmatrix} \tag{2.14}$$

Where x_d and z_d define the position on the detector plane and the distances of propagation of the two plane waves are defined as r_1 and r_2 respectively.

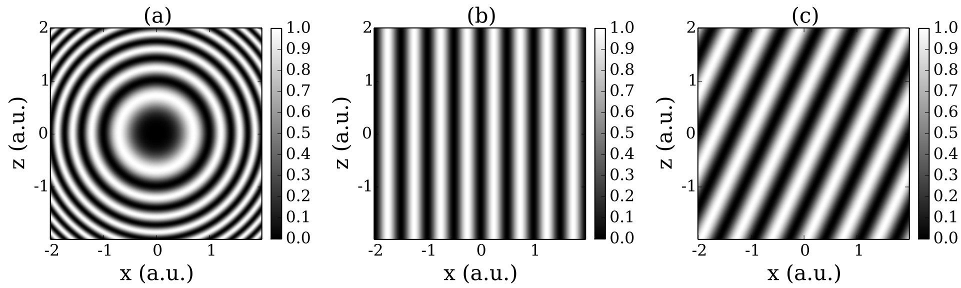

Fig. 2.1: Comparison between the different types of interference pattern that can be observed using a Michelson interferometer. (a) shows the circular fringes created by Gaussian beams propagating in the same direction. The striped fringes in (b) are a result of one wave being titled in respect to the y-axis and the tilted stripes in (c) are a result of one wave being tilted in respect to the y-/z-axis.

The phase difference $\Delta\varphi(\mathbf{r}_d)$ can now be calculated:

$$\begin{aligned}\Delta\varphi(\mathbf{r}_d) = \mathbf{k}_1 \cdot \mathbf{r}_1 - \mathbf{k}_1 \cdot \mathbf{r}_1 &= \frac{2\pi}{\lambda}\left(\begin{pmatrix}\sin(\alpha)\\ \cos(\alpha)\\ 0\end{pmatrix} \cdot \begin{pmatrix}x_d\\ r_1\\ z_d\end{pmatrix} - \begin{pmatrix}0\\ 1\\ 0\end{pmatrix} \cdot \begin{pmatrix}x_d\\ r_2\\ z_d\end{pmatrix}\right) \\ &= \frac{2\pi}{\lambda}\sin(\alpha) \cdot x_d - \frac{2\pi}{\lambda}\left(\cos(\alpha) r_1 - r_2\right) \\ &= \underbrace{\frac{2\pi}{\lambda_0} n \sin(\alpha) \cdot x_d}_{\varphi(x_d)} - \underbrace{\frac{2\pi}{\lambda_0} n \left(\cos(\alpha) r_1 - r_2\right)}_{\varphi_0}\end{aligned} \tag{2.15}$$

The phase difference consists of the term $\varphi(x_d)$, which depends on the x-position on the detector plane, and the tilt angle α, as well as a constant term φ_0, which depends on the OPD and the tilt angle α. Also the phase difference is independent of the z-position on the detector plane. Inserting $\Delta\varphi$ into equation (2.10) leads to the formation of striped fringes on the detector plane:

$$\bar{I} \propto E_0^2 \cdot \left[1 + \cos(\varphi_{x_d})\cos(\varphi_0) - \sin(\varphi_{x_d})\sin(\varphi_0)\right] \tag{2.16}$$

The distance between to interference fringes can be controlled by increasing or decreasing the tilt angle α of the mirror. Figure 2.1 (b) shows such a fringe pattern.
In an even more general case where the mirror is not only tilted in respect to the y-axis but also in respect to the z-axis an additional term $\varphi(z_d)$ will lead to the stripes being tilted as is depicted in figure. 2.1 (c).

2.3. Dispersion and refractive index

Dispersion describes the phenomenon of the frequency dependence of the phase velocity υ_{ph} of light waves propagating through a medium.

$$\upsilon_{\text{ph}}(\lambda) = \frac{c}{n(\lambda)} \tag{2.17}$$

The factor n is called the refractive index and it depends on the wavelength λ. Using the plane wave expression described in equation (2.5) we get

$$\mathbf{E}(t,z) = \mathbf{E}_0 \cdot \exp\left(i\omega(t - z/\upsilon_{\text{ph}})\right) . \tag{2.18}$$

While the frequency ω stays constant, the wavelength λ inside the medium gets a factor n smaller. This can be described classically as a primary wave (the incoming wave) which drives harmonic oscillations of the electrons surrounding the atoms. These oscillating dipoles emit electromagnetic waves with the same frequency but with a delayed phase response (secondary waves). When observing the wave at a point behind the medium the superposition of these waves leads to

$$\mathbf{E}(z) = \underbrace{\mathbf{E}_0 \exp\left(i\omega t - \frac{\omega z}{c}\right)}_{\mathbf{E}_i} - \underbrace{i\omega(n-1)\frac{\Delta z}{c}\mathbf{E}_0 \exp\left(i\omega t - \frac{\omega z}{c}\right)}_{\mathbf{E}_r} \tag{2.19}$$

with the thickness of the medium Δz [20]. $\mathbf{E}_i$ describes the electric field of the incoming plane wave while the second term $\mathbf{E}_r$ describes the electric field response of the medium, which can be understood as the superposition of all the electromagnetic waves emitted by the oscillating dipoles. The waves emitted by the oscillation of these dipoles can also be described approximately by first solving the differential equation of a driven harmonic oscillator describing their motion and then calculate the resulting fields.

$$m\left(\ddot{\mathbf{r}} + \Gamma\dot{\mathbf{r}} + \omega_0^2\mathbf{r}\right) = f(t) \tag{2.20}$$

With a periodic force $f(t)$ driving the oscillation. The electric field of the light wave is exerting a force $\mathbf{F}(t) = -e \cdot \mathbf{E}(t) = -e\mathbf{E}_0 \exp(i\omega t)$ on the electron. Solving the differential equation using this periodic force, the solution reads [22]

$$\mathbf{r}(t) = -\frac{e\mathbf{E}_0}{m}\left(\frac{\exp(i\omega t)}{\omega_0^2 - \omega^2 - i\omega\Gamma}\right) . \tag{2.21}$$

The oscillating dipoles posses a time-dependent dipole moment $\mathbf{p}(t) = -e \cdot \mathbf{r}(t)$ and create a vector potential $\mathbf{A}(\mathbf{r},t) \propto \mathrm{d}/\mathrm{d}t\, \mathbf{p}(t - r/c)$ [22]. This time-dependent vector potential generates a temporally variable electromagnetic field. By integrating over all fields emitted by all oscillating dipoles in the medium and using eq. (2.21) to describe their motion the resulting field at a point behind the medium can be described by

$$\mathbf{E}_r(z) = -i\omega\frac{\Delta z}{c} \cdot \frac{\rho e^2}{2\epsilon_0 m\left[(\omega_0^2 - \omega^2) + i\omega\Gamma\right]} \cdot \mathbf{E}_0 \exp\left(i\omega t - \frac{\omega z}{c}\right) . \tag{2.22}$$

Where ρ is the density of oscillating dipoles in the medium.
Comparing this equation with the term $\mathbf{E_r}$ in (2.19) yields the refractive index [4]

$$
\begin{aligned}
n &= 1 + \frac{\rho e^2}{2\epsilon_0 m\left[(\omega_0^2 - \omega^2) + i\omega\Gamma\right]} \\
&= 1 + \frac{\rho e^2}{2\epsilon_0 m} \cdot \frac{(\omega_0^2 - \omega^2) - i\omega\Gamma}{(\omega_0^2 - \omega^2)^2 - \omega^2\Gamma^2} \\
&= n_r(\omega) - i\kappa(\omega)\,.
\end{aligned}
\tag{2.23}
$$

The real part of n called the refractive index $n_r(\omega)$ while the imaginary part $\kappa(\omega)$ is called the extinction coefficient.

2.3.1. Empirical formulas for calculating the refractive index of air

As the beams used to generate the optical superlattice propagate through air it is of great importance to understand how the refractive index of air changes with changing environmental conditions. Calculating the refractive index of air for different environmental condition is not viable using equation (2.23). But many different empirical formulas for calculating the refractive index of air exist [5]. The one used in this thesis, the *modified Edlén* equation was published in 1998 by G. Bönsch et. al who revised the work done by Edlén in 1966 [6][24].

$$
n_r(\lambda) = n_{tp} - 10^{-10}\left[(292.75/(T + 273.15)) \cdot (3.7345 - 0.0401 \cdot \frac{1}{\lambda^2})\right] \cdot p_v \tag{2.24}
$$

where n_{tp} is the part of the refractive index depending on temperature and pressure and p_v is the partial pressure of the water vapor dependent on the relative humidity RH and the temperature. A detailed description of the computation of the refractive index using the modified Edlén equation is given in Appendix B figure. In their work Bönsch et. al expect the relative measurement uncertainty of their modified Edlén equation to be on the order of 10^{-8}. But the accuracy of the calculation depends heavily on the accuracy with which the environmental parameters are measured [25]. The variation of refractive index for different wavelengths is calculated using equation (2.24) and is shown in figure 2.2. Towards the ultraviolet part of the spectrum, the dispersion of air gets steeper. As the planned superlattice uses ultraviolet (362 nm) and red (724 nm) light it will be working right at the steeper region of the dispersion of air. As a result of this, the change in refractive index affects the superlattice more heavily than it would for example for infrared wavelengths where the dispersion in air is flattened.

[4] This derivation is only valid for an optically thin medium (i.e. air) where $(n-1) \ll 1$ [20].
[5] Because the refractive index of air is of great interest for astronomy and meteorology many formulas for calculating the refractive index of air exist.
[6] In 1966 Edlén re-did his previous work done in 1953 [23].

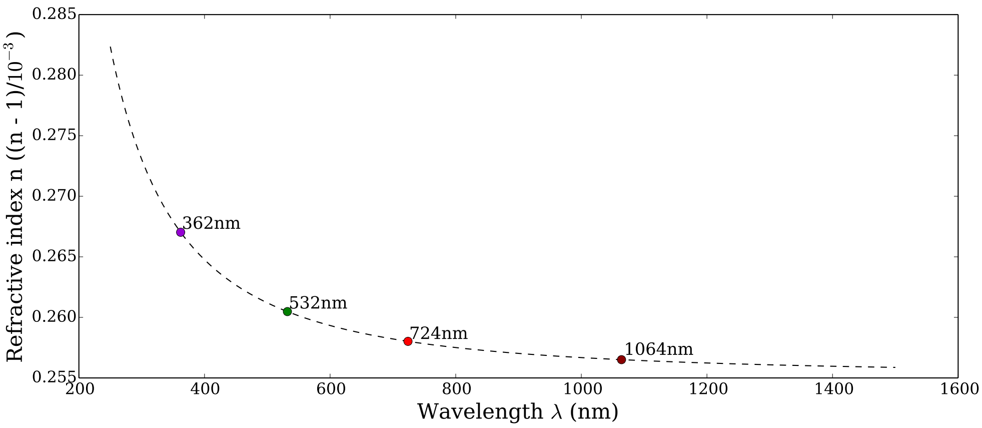

Fig. 2.2: Dispersion of air for a temperature $T = 24\,°\mathrm{C}$, a pressure $p = 990\,\mathrm{hPa}$ and a relative humidity of $RH = 40\,\%$. For selected wavelengths the position of the refractive index is marked.

2.4. Optical Lattices

Optical lattices are formed by the interference of two beams of light creating a spatially periodic interference pattern i.e. a standing wave. This can be achieved by retro-reflecting a coherent beam back into itself. Doing so creates two counter-propagating beams where $\mathbf{k}_1 = -\mathbf{k}_2$, $\mathbf{r} = \mathbf{e}_y$ and $\omega_1 = \omega_2 = \omega$. The phase difference reads

$$\Delta\varphi = (\mathbf{k}_1 \cdot \mathbf{r} + \varphi_1) - (-\mathbf{k}_2 \cdot \mathbf{r} + \varphi_2) = 2k \cdot y + \Phi \tag{2.25}$$

where $k = 2\pi/\lambda$ and Φ is the relative phase difference between the two beams. Inserting this expression for $\Delta\varphi$ into equation (2.10) leads to

$$\bar{I} \propto E_0^2 \cdot [1 + \cos(2k \cdot y + \Phi)] \tag{2.26}$$

In contrast to the case where the two beam propagate in the same direction, two counter-propagating beams create a standing wave that is modulated along the direction of the wave propagation. Such a standing wave is depicted in figure 2.3 (a). The spatial period of a standing wave formed this way only depends on the wavelength of the beams. Another way of creating standing waves is to intersect two beams under an angle α. This results in an interference pattern resembling a standing wave that modulates perpendicular to the direction of wave propagation [7]. The period of standing waves created this way is only dependent on the angle α under which the two beams intersect and can thus be controlled by changing α. A standing wave with variable period is also called an *accordion lattice* [26].

So far only optical lattices in one dimension were described. Optical lattices in two dimensions (figure 2.3 (b)) can be realized by superimposing two non-interfering standing waves[8]. Interference between the two standing waves can be avoided by choosing orthogonal polarizations or a sufficiently large detuning [28]. The resulting intensity pattern created by two superimposed standing waves can be written as

$$I(\mathbf{r}) = A_1 \cos^2(\mathbf{k}_1\mathbf{r} + \varphi_1) + A_2 \cos^2(\mathbf{k}_2\mathbf{r} + \varphi_2)\,. \tag{2.27}$$

Where A_1 and A_2 are the amplitudes of the individual standing waves and φ_1 and φ_2 are the phases of the respective standing waves. Thus in order to achieve a stationary lattice pattern the phase between the superimposed standing waves has to be stabilized.

[7] This was already discussed in detail in section 2.2.

[8] By allowing the standing waves to interfere Uehlinger et al. generated a more complex lattice geometry[27]

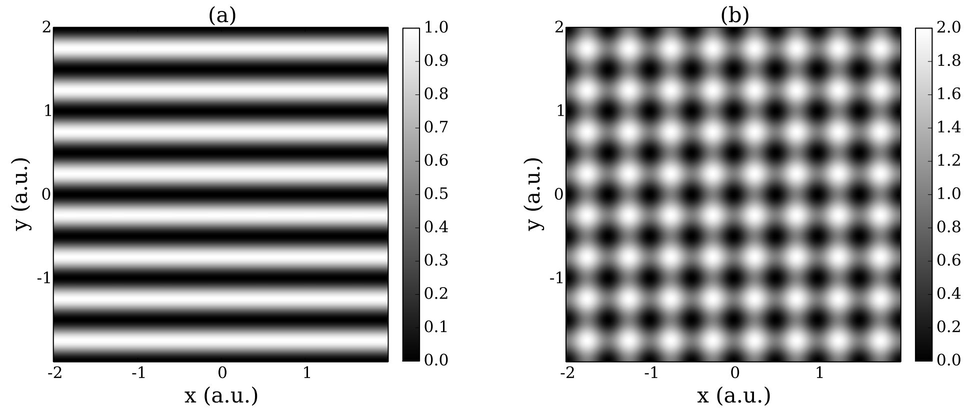

Fig. 2.3: Intensity pattern of an one-dimensional lattice (a) and a two-dimensional lattice (b). Regions of high intensity are depicted in white, while regions of low intensity are dark.

2.5. Optical superlattices

Optical superlattices are created by superimposing a lattice with a short lattice period (short lattice) and another lattice with a long lattice period (long lattice) in order to create more complex periodic interference patterns. Figure 2.4 shows the gradual emergence of a superlattice where the spatial period of the short lattice is half that of the long lattice. Between the different figures 2.4(a), (b) and (c) the amplitude of the short lattice was increased. The behavior of the superlattice for different relative phases Θ between the two lattices is depicted in figure 2.5. In the case of a superlattice where the short lattice has twice the spatial periodicity as the long lattice ($k_1 = 2k_2$), a symmetric double well potential can be observed at $\Theta = 0$. While at $\Theta = \pi/4$ the superlattice shows an antisymmetric double well configuration. The intensity pattern of the superlattice where $A_1 = A_2$ and $k_1 = 2k_2$ can be calculated using equation (2.27).

$$\begin{aligned} \bar{I} &\propto \cos^2\left(2k_2\mathbf{r} + \varphi_1\right) + \cos^2\left(k_2\mathbf{r} + \varphi_2\right) \\ &= \frac{1}{2}\left[2 + 2\cos(3k_2\mathbf{r} + \varphi_1 + \varphi_2)\cos(k_2\mathbf{r} + \varphi_1 - \varphi_2)\right] \end{aligned} \tag{2.28}$$

The intensity pattern consist of a fast oscillating cosine function and a slow oscillating one. The information about the superlattice geometry is contained in the slow oscillating cosine function with a relative phase $\Theta' = \varphi_1 - \varphi_2$. Because $\cos^2(x)$ has a π-periodicity while $\cos^2(2x)$ has a $\pi/2$-periodicity φ_1 and φ_2 are not defined in the same domain. In order to calculate the relative phase Θ between the two interference pattern this has to be taken into account yielding

$$\Theta = 0.5 \cdot \varphi_{2x} - \varphi_x \,. \tag{2.29}$$

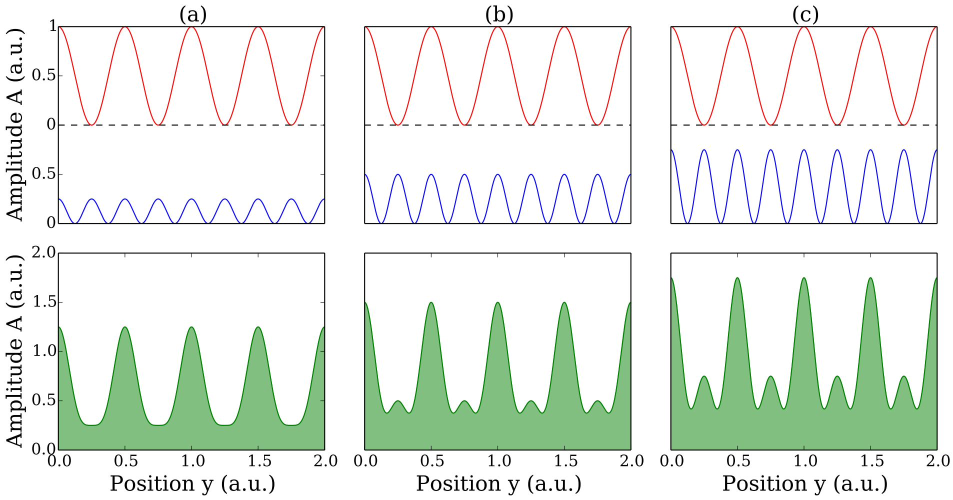

Fig. 2.4: Emergence a superlattice with $2\lambda_1 = \lambda_2$ for different amplitudes of the short lattice. The amplitude of the short lattice is 0.25, 0.5 and 0.75 times the amplitude of the long lattice for (a) (b) and (c), receptively. The relative phase $\Theta = 0$ stays constant for all figures.

Where φ_{2x} is the phase of the short lattice and φ_x being the phase of the long lattice [9]. This behavior is also depicted in figure 2.6. Both examples result in a superlattice with an antisymmetric double well configuration. Using the equations (2.28) and (2.29) this is to be expected since both examples give the same relative phase $\Theta = 0.25\pi$. However they do not give the same image since there is a phase $\varphi_1 + \varphi_2$ in the fast oscillating cosine function which changes between the two examples.

[9] This is only the case where $k_1 = 2k_2$, for other combinations of wave vectors this relative phase has to be calculated accordingly.

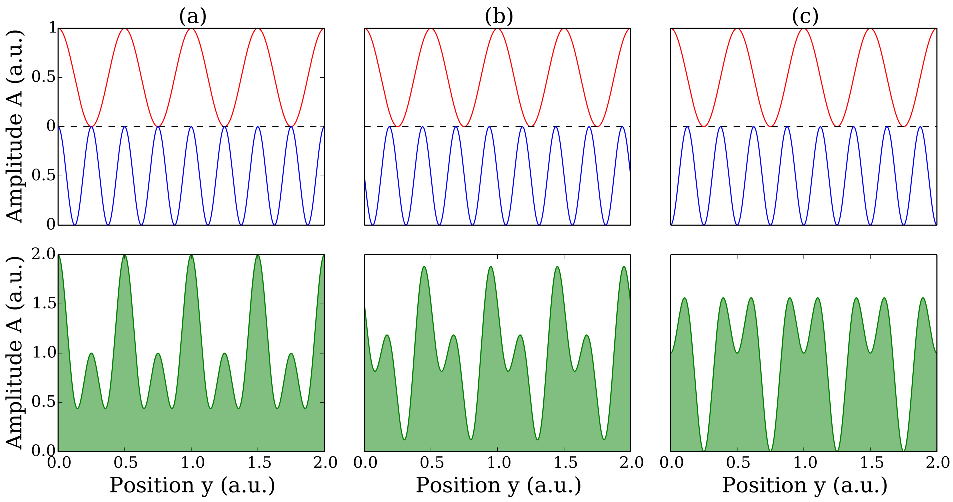

Fig. 2.5: Amplitude of the superlattice with $2\lambda_1 = \lambda_2$ for different relative phases. Both sub lattices have equal amplitudes. The relative phase between the two lattices is $\Theta = 0$, $\Theta = \pi/8$ and $\Theta = \pi/4$ for (a), (b) and (c), respectively.

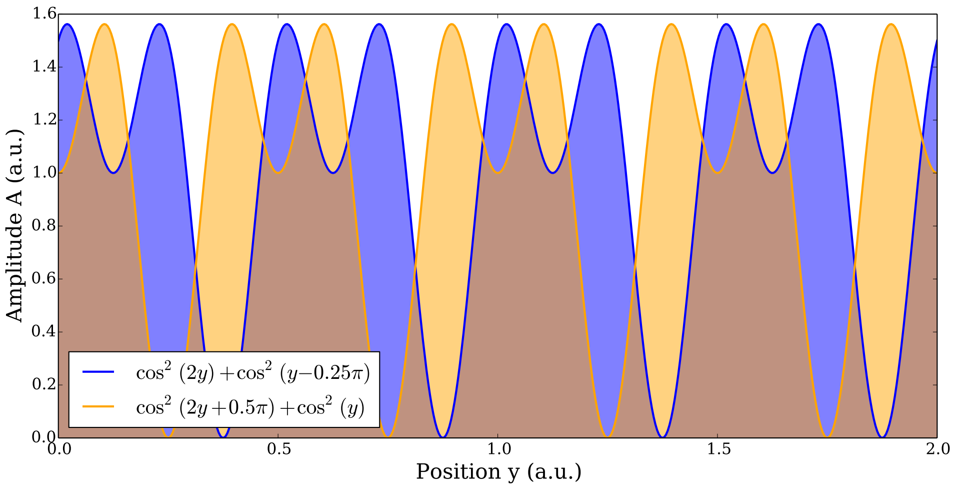

Fig. 2.6: Two different possibilities of creating the same superlattice configuration.

2.6. Michelson interferometer

An interferometer makes use of the interference by purposefully superimposing coherent light beams to extract information [10].

The Michelson interferometer, invented by Albert Abraham MICHELSON is a common and very simple type of interferometer. An incoming, coherent light source is split into two arms. After propagating a certain distance both arms are retro-reflected back and detected on a common plane. Fig. 2.7 shows a schematic drawing of such a setup. Because of their great precision interferometers are widely used in science and industry. For example, the *Laser Interferometer Gravitational-Wave Observatory* (LIGO) uses a Michelson interferometer setup to detect displacements in optical path length less than a thousandths of the diameter of the proton over a distance of 4 km [31]. Michelson interferometers can also be used to probe the refractive index of materials. By placing the unknown material in the optical path of one of the arms, light that propagates through the material experiences a phase delay depending on the thickness and refractive index of the material. Because the light propagation in the other arm does not experience this phase shift the interference pattern changes. By measuring this change the refractive index of the unknown material can be calculated. In this thesis a Michelson interferometer is used as a means to test the phase stability of the planned optical superlattice. It is used to detect the relative phase between two independent interference pattern (lattices) induced by changes in their optical path difference

$$\Lambda = n\left(|\Delta r|\right) . \tag{2.30}$$

These changes can be caused by either a change in the spatial path length Δr, for example due to thermal expansion, or by changes in the refractive index n caused by changing environmental conditions.

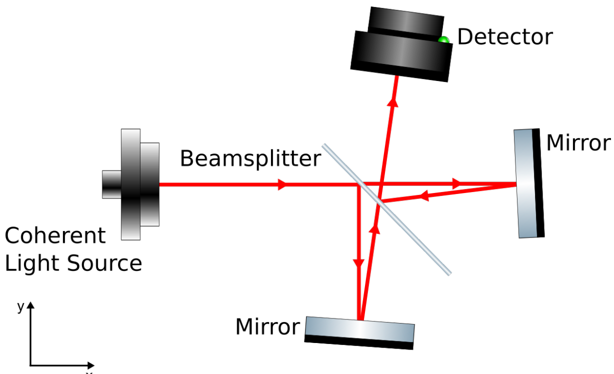

Fig. 2.7: Schematic drawing of a Michelson interferometer setup. The angle of incident at the mirrors is exaggerated in order to better differentiate between incoming and reflected beams.

[10]under certain conditions incoherent light sources can also be used [29, 30]

3. Stability of the Optical Superlattice

It has been established that the stability of a two-dimensional optical lattice is dependent on phase between the two superimposed standing waves (2.27) (if $\mathbf{k}_1 \| \mathbf{k}_2$) which itself is dependent on the optical path difference between the two beams creating the standing wave (2.15). In order to achieve a stationary superlattice the relative phase Θ between the short and the long lattice therefore has to be stabilized.
Since the long and the short lattice share their optics their spatial path difference is constant and the optical path difference depends only on the refractive index which, due to dispersion, is different for the different wavelengths. Because the refractive index changes with changing environmental conditions, so does the optical path difference and therefore the relative phase. Figure 3.1 shows this change in relative phase Θ of the planned superlattice with a wavelength for the short lattice of 362 nm and 724 nm for the long lattice, calculated for different environmental conditions. The relative phase can be calculated using

$$\varphi_i = \frac{2\pi n_i \ell_i}{\lambda_i} \tag{3.1}$$

and equation (2.29). Using $\ell_1 = \ell_2 = \ell$ and $2\lambda_1 = \lambda_2$ yields:

$$\Theta = \frac{\pi \ell}{\lambda_1} \cdot (n_1 - n_2) \tag{3.2}$$

Where n_i is the refractive index calculated via the modified Edlén equation and the measured environmental data, ℓ_i is the spatial path length and λ_i is the wavelength.
In order to see how much the environmental conditions inside the laboratory (lab) are expected to change, the temperature, pressure and relative humidity is monitored over a period of one day. This environmental data is depicted in figure 3.2. During the night time with most of the machines turned off the temperature decreases. In the morning when people start working in the lab the temperature increases again. The same is true for the relative humidity inside the lab but the changes are smaller because the dehumidifiers inside the lab run at a stretch. This seems reasonable as the chillers needed for the lasers and other equipment are located inside the lab and therefore affect the temperature in the lab. The pressure however seems to change independently. Because the lab is not sealed airtight the pressure inside equalizes with the surrounding pressure. While the absolute changes of the environmental conditions are not that big they cannot be neglected as even small changes in relative phase Θ will change the superlattice geometry and therefore change the trap depth in neighboring wells of the superlattice potential [11]. In order to illustrate this, figure 3.1 shows the superlattice geometry for different relative phases Θ. The expected change of Θ throughout the day is shown in figure 3.2. The relative phase is calculated using only the respective environmental factors. For example, the Θ shown in figure 3.2(a) is calculated only taking into account the change in temperature while all the other values stay constant. Θ_0 is always calculated using the fist data point of the temperature, pressure and humidity.

[11] In [32] it is stated that a phase change of $\Delta\Theta = 0{,}05\pi$ will severely affect the manipulation of the atoms trapped in the lattice.

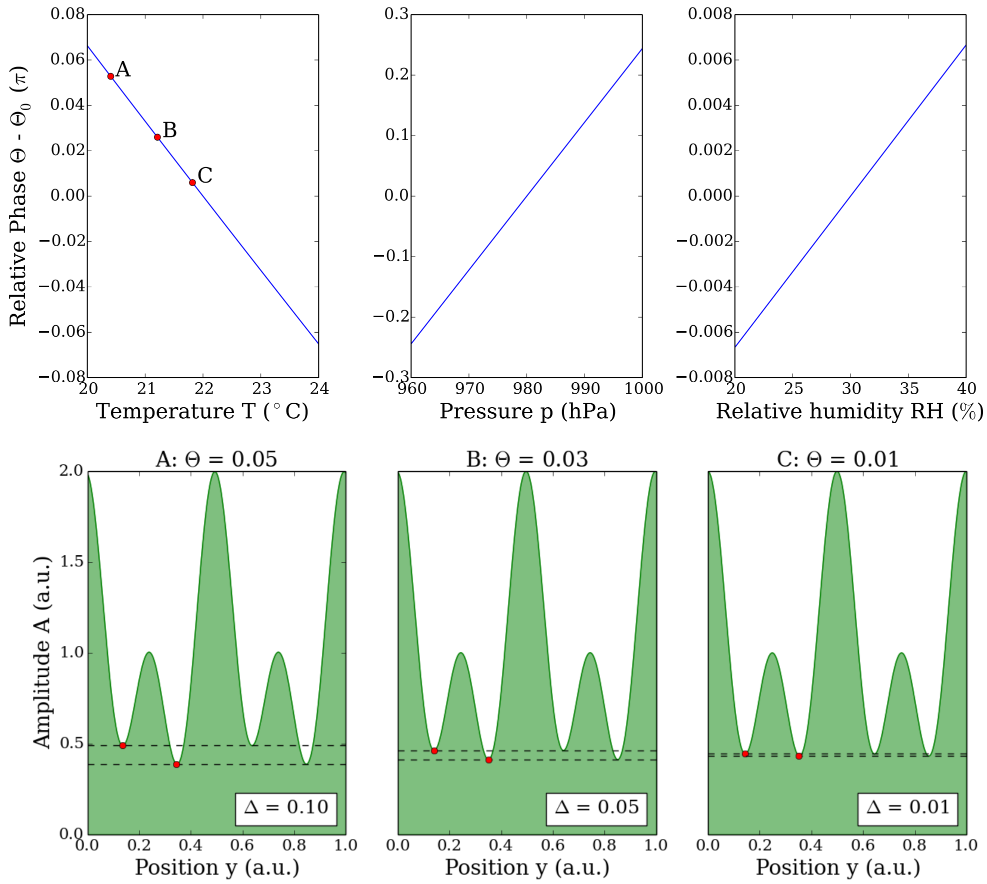

Fig. 3.1: The relative phase Θ between the two lattices (362 nm and 724 nm) in units of π is calculated for changing temperatures, pressures and relative humidity. Θ_0 is calculated at $T = 22\,°\mathrm{C}$, $p = 1000\,\mathrm{hPa}$ and $RH = 40\,\%$ and is shown the upper figures. The spatial path distance of the beams in air was set to $\ell = 0.40\,\mathrm{m}$. The points A, B and C mark the position of the three plots shown below. For these three different values of relative phase Θ, the difference in potential depth is calculated and is also depicted in the plots below.

3.1. Experimental setup

The phase stability of the superlattice is tested using a Michelson interferometer setup like the one shown in figure 3.3. The working part of the interferometer is enclosed inside a paper box to protect it from the air flow produced by the climate control located above the breadboard or people walking by the experiment. The red light at 724 nm is produced by an M-Squared SolsTis system. It is pumped via a diode-pumped solid state laser providing 18 W at 532 nm[12]. The ultraviolet light at 362 nm is made by second harmonic generation (SHG) of the red light using the M-Squared SolsTis ECD-X module. A schematic drawing of the laser setup is depicted in Appendix A, figure A.1.

[12] Lighthouse photonics - Sprout-G 18W

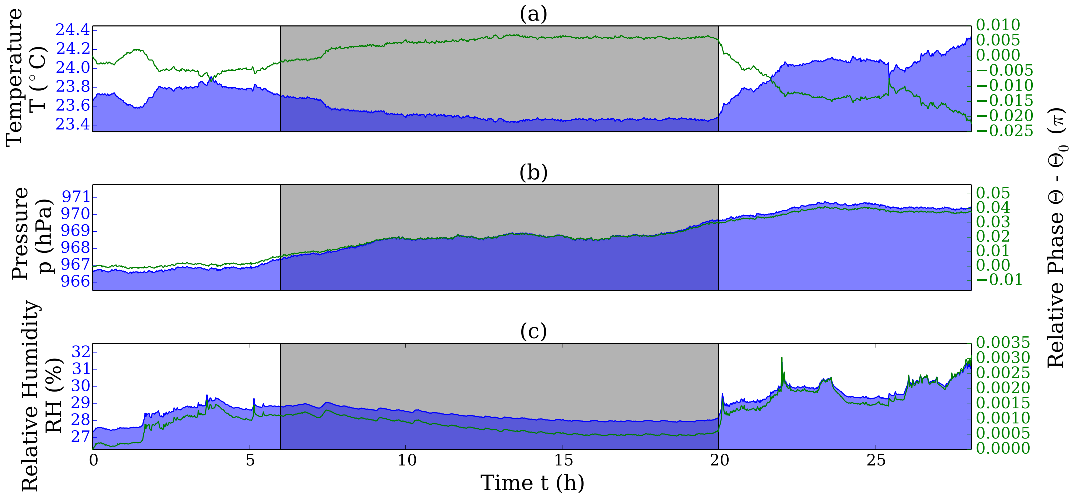

Fig. 3.2: Environmental data inside the lab collected over the course of 24 h. The gray area marks the night time. The relative phase Θ_0 is calculated using the first data points. Θ only takes changes in the respective measurement into account. Through this measurement it becomes clear that changes in the relative phase throughout the day can on the order of $0.05\,\pi$.

The Michelson interferometer is first aligned using only the ultraviolet light. This is done by first ensuring that the beam is straight and collimated using the telescope while also adjusting the dichroic mirror (DCM) and M3. The purpose of the telescope is to increase the spot size of the ultraviolet beam while also lowering the intensity. Next, the beamsplitter is mounted such that the incoming beam has a 45° angle of incident. M4 and M5 are adjusted until vertical interference fringes can be observed on the the camera. Afterwards the red and the ultraviolet light are superimposed at the dichroic mirror using only the mirrors M1 and M2 to adjust the red light. The alignment is successful as soon as vertical interference fringes can be observed for both wavelengths. Figure 3.4 shows the comparison between a bad alignment where the fringes of the two interference patterns are not parallel and a good alignment where the fringes are parallel[13]. The spacing of the long lattice is twice that of the short one. The environmental data is monitored using a BME280 sensor from Adafruit connected to a Teensy 3.2. Both the camera and the sensor are controlled using MATLAB. To ensure that the recorded images can be assigned to their environmental data and to get accurate intervals between two images both the images and the environmental data are stored with a time-stamp.

[13] The two fringe pattern do not necessarily have to overlap as long as they are parallel.

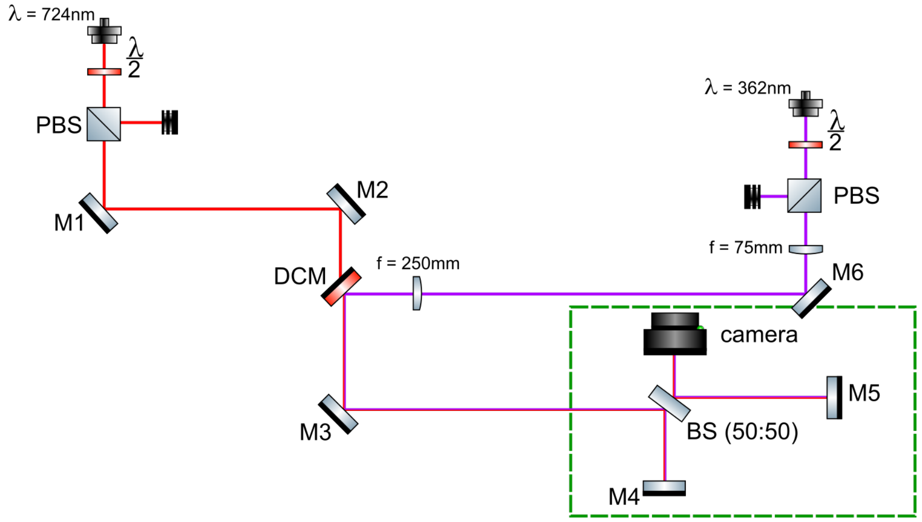

Fig. 3.3: Schematic drawing of the optical setup. The green box surrounds the working part of the Michelson interferometer. The mirrros used are: M1, M2 (Thorlabs: BB1-E02), DCM (Thorlabs: DMLP-425), M3 - M5 (Thorlabs: PF10-03-P01) and M6 (Lens-Optics: M365/1"/45). The beamsplitter used is a plate beamsplitter from Thorlabs (BSW10).The camera is a Webcam Pro 9000 from Logitech.

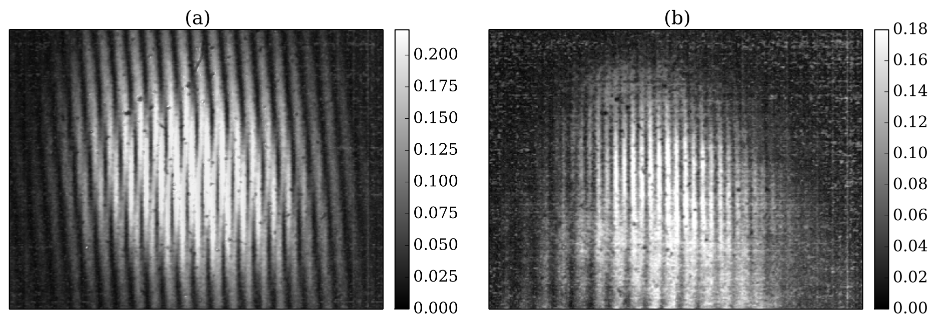

Fig. 3.4: Comparison between a bad alignment shown in (a) where the two fringe pattern are not parallel to each other and a good alignment (b) where both pattern are parallel and overlap each other

3.1.1. Plate beamsplitter and ghosting

Because a non polarizing beamsplitter cube with an anti-reflection coating suitable for both the ultraviolet and the red wavelength is not commercially available, a plate beamsplitter from Thorlabs (BSW10) is used instead. This has the disadvantage that second order reflections, also called *ghosting*, can occur at the backside of the plate beamsplitter. This behavior is shown in figure 3.5. While normally undesirable, in this application ghosting is necessary in order to properly overlap the two beams. Because the second order reflection has reduced intensity the two interfering plane waves have different intensities.
One side of the beamsplitter is coated using the beamsplitter coating. Because ghosting usually is to be avoided the other side has an anti-reflection coating[14] which suppresses the ghosting. Additionally the AR-coated side of the beamsplitter has a 30 arcmin wedge to ensure that the ghosting that is still present diverges [33]. As a result of this, the intensity of the light detected at the camera is reduced to less than one percent. Also, to counteract the divergence of the ghosting induced by the wedge, the mirror has to be tilted resulting in a stripe pattern [15]. Despite these limitations the plate beamsplitter works fine in the interferometer setup and the results look as expected.

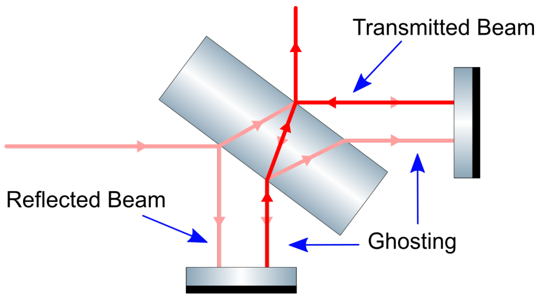

Fig. 3.5: Schematic drawing of a plate beamsplitter. The pale lines show the beam path while the saturated lines show the part of the beam that interferes at the camera.

3.2. Extracting the phase information

As the task of this thesis is to test the phase stability of the superlattice setup, the phase information gathered using the Michelson interferometer setup has to be extracted. With this setup images like the ones depicted in figure 3.6 (a) are recorded with an image size of 640 x 480 pixels and a pixel-size of 7.04 µm.
In order to extract this phase information the data is first integrated over the y-axis of the image in order to obtain the x-profile of the image data like the one shown in figure 3.6 (b). This presupposes a good alignment of the interference patterns where both patterns are parallel. Because the interference pattern is created using beams that have a gaussian intensity profile, the x-profile has a gaussian envelope. In comparison, the different superlattice configurations shown in the figures 2.5 (a)-(c) are calculated

[14] approx. 1% reflectance at 45° AOI
[15] An active stabilization of the phase using a photo diode is only possible for circular interference fringes.

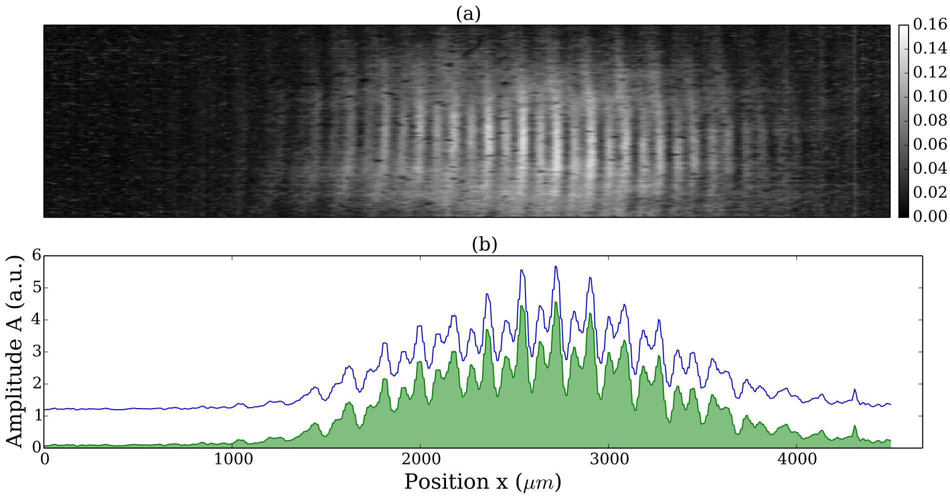

Fig. 3.6: The recorded image data is depicted in (a). In (b) the green area marks the x-profile while the blue curve is calculated using equation 3.3.

using plane waves and lack this intensity envelope. Using the discrete Fourier transform (DFT) one has access to the amplitude and the phase of the different complex frequency components of finite data set (in this case the x-profile of the image). The DFT expresses the original data as the sum of periodic functions. The fast Fourier transformation (FFT) is a discrete Fourier transform using a very fast algorithm, published by Cooley and Tukey in 1965 [34]. Using the Fourier transform to calculate both the amplitude and the phase of each frequency component, the original data can be recovered as the sum of periodic functions.

$$f(x) = \sum_{n=0}^{N} A_n \cdot \cos(f_n \cdot 2\pi \cdot x + \phi_n) \tag{3.3}$$

Where A_n is the amplitude, ϕ_n is the phase, f_n is the corresponding frequency and N is the length of the data set.
One can exploit the symmetry of the Fourier transform and restrict its outputs to positive frequencies up to and including the Nyquist frequency $f_N = 0.5 \cdot f_S$ [35]. Where the maximum sampling frequency $f_S = 1/T_S$ is calculated via the sampling rate $T_S = 7.04\,\mu\text{m}$. The sampling rate fixed by the pixel-size of the camera. The resolution of the Fourier transform is given by

$$\Delta f = \frac{f_S}{N}\,. \tag{3.4}$$

The resolution of the Fourier transform is important because in order to accurately extract the phase information the frequency of the red and the ultraviolet lattices have to be determined with as much precision as possible. In order to reduce the impact of the finite resolution, the lattice spacing on the camera is chosen to be on the order of 100 µm.

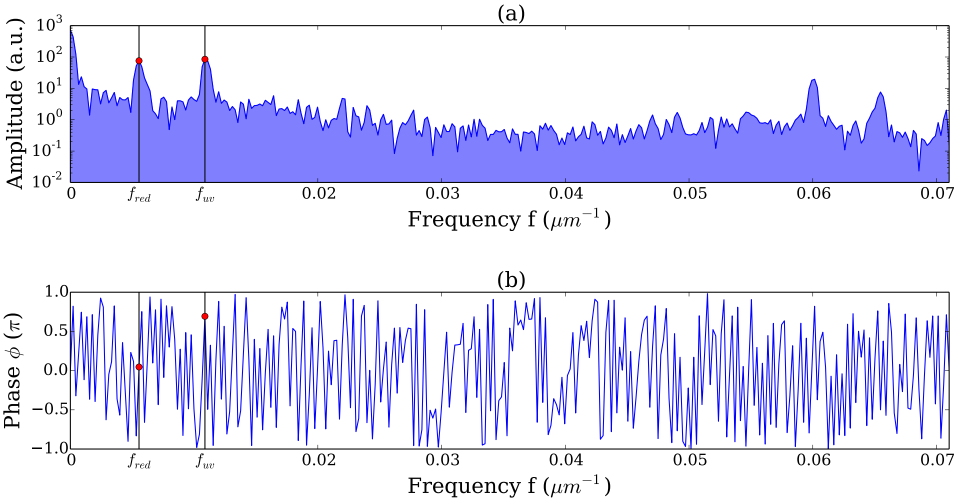

Fig. 3.7: The discrete Fourier transform of the x-profile is calculated in order to access the amplitude and phase of each frequency component. The amplitude spectrum is shown in (a) and the phase spectrum is shown in (b). Because the phase is calculated in an interval between $(-\pi, \pi]$, a phase of $\phi = 1$ is equivalent to a phase of $\phi = -1$. The red dots mark the position of the frequencies corresponding to the red and ultraviolet interference pattern respectively.

3.3. Results

In order to evaluate the stability of the superlattice the phase of the individual lattices are measured using the method described above. The measurements are then compared to the theoretical expectations using the modified Edlén equation.

3.3.1. Ideal case

The following measurement is done overnight to minimize large fluctuations and after the enclosed interferometer-setup had time to thermalize. These measures are being taken in order to achieve an ideal environment for the setup where only the change of air pressure and humidity affect the phase of the lattices. An example of such a measurement is shown in figure 3.8. Each line represents the x-profile of a single image. The calculated phase of the individual lattices is depicted in figure 3.9(a). The Fourier transform outputs the phase information in an interval between $(-\pi, \pi]$. As the camera measures the intensity, which has a π periodicity, the phase is then multiplied by a factor of 0.5. To account for π-jumps in the phase and the fact that the camera is mounted upside down, the phase data is then adjusted accordingly and shown in figure 3.9(b). The relative phase is calculated using equation 2.29 and is depicted in figure 3.9(c). The environmental data from inside the enclosed interferometer setup corresponding to the measured phase data is shown in figure 3.10(a)-(c). During the measurement, the temperature changes only slightly. Therefore thermal expansion of mirror mounts can be neglected. The pressure steadily increases by about 0.5 hPa/h during the whole measurement. A change in the

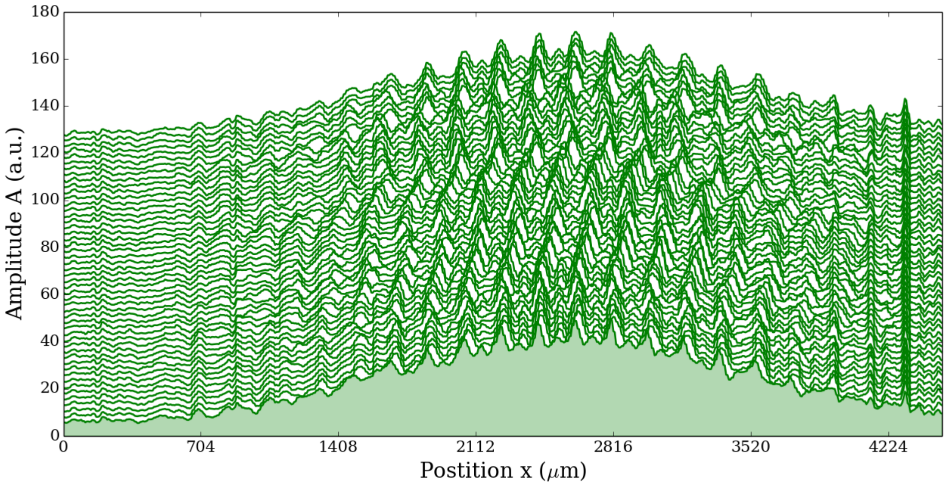

Fig. 3.8: Each line represents the x-profile of a single image. The interval between two images is $T_{\text{int.}} \simeq 90\,\text{s}$ while the interval between two lines is approx. 13 min and 50 out of the 450 images are depicted.

phase can therefore only be caused by the change in pressure. The calculations show that the impact of a change in relative humidity can be neglected compared to the the influence of pressure and temperature (see also fig. 3.1). Figure 3.11 shows a comparison between the experimental data and the theoretical predictions using calculation via the modified Edlén equation. The overall phase change of the individual lattices for the experimental data as well as the theoretical prediction follows the same trend and is about $2\,\pi$ for the ultraviolet light and π for the red light (Fig. 3.11(a), (c)). In the beginning of the measurement the relative phase shows a similar trend for both the experimental data and the theoretical prediction. Starting at around the 6 h mark the experimental data and the theoretical prediction diverge and follow different trends.

The measurement shows that, thermal expansion can be neglected during the measurement. The phase change caused by a change of optical path distance is manly due to the change in refractive index and can be predicted reasonably well using the modified Edlén equation.

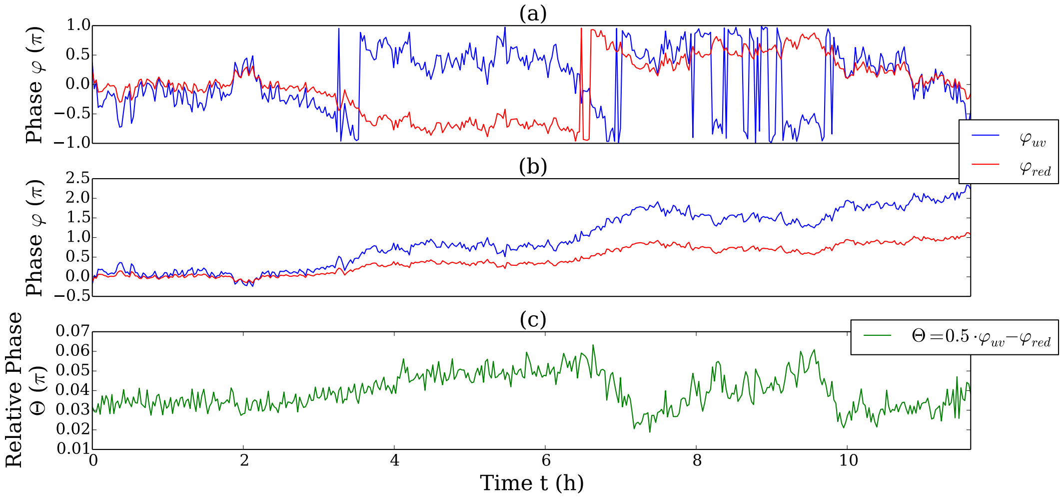

Fig. 3.9: Phase φ of the individual lattices calculated via the Fourier transform method (a) and the data adjusted for 2π-jumps and multiplied by a factor of -1 (b). The relative phase Θ is calculated using the unadjusted data and is depicted in (c). The interval between two data points is $T_{\text{int.}} \simeq 90\,\text{s}$ and the spatial path length the beam has to propagates through is $\ell \simeq 0.4\,\text{m}$.

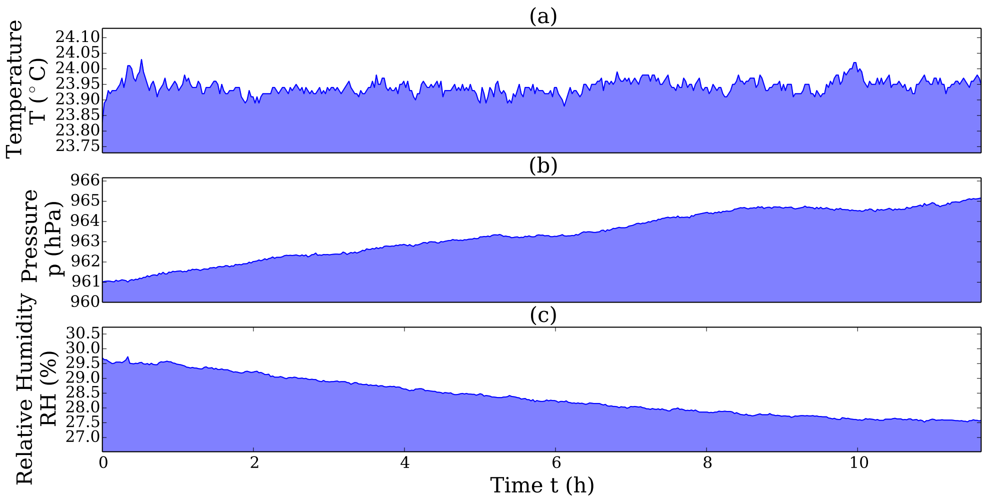

Fig. 3.10: Environmental data measured via the sensor inside the enclosure around the Michelson interferometer corresponding to the measurement depicted in figure 3.9. The interval between two data points is again approx. 90 s. Sub-figure (a) shows the temperature T, (b) shows the pressure p and (c) shows the relative humidity RH.

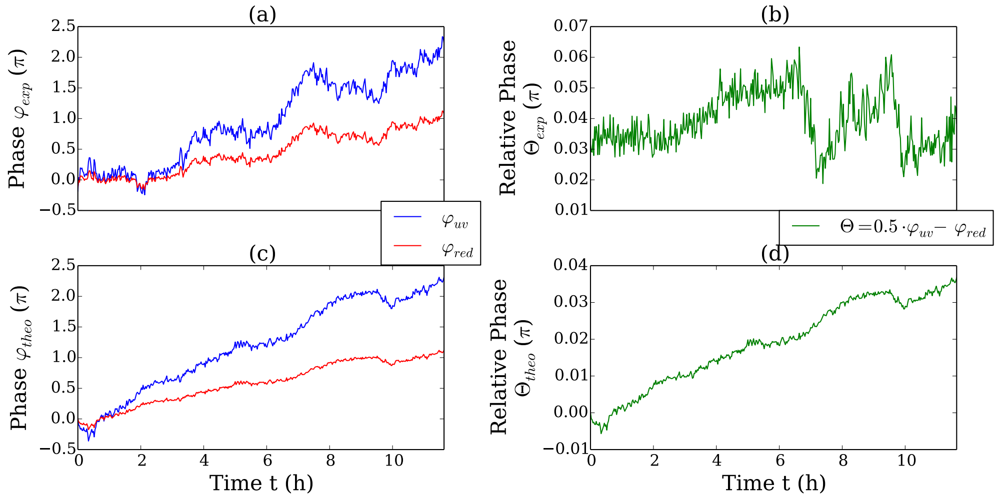

Fig. 3.11: Comparison between the experimental data (a) and (b) and the theoretical predictions calculated via the modified Edlén equation (c) and (d) corresponding to the measurement depicted in figure 3.9 and the environmental data shown in figure 3.10.

3.3.2. External heating of the setup

These measurements are done during the day with people working in the lab and with a coil that is actively heating up the enclosed interferometer setup. This is a more realistic case of measuring the stability of the superlattice setup. In the new experiment the superlattice will be located at the science chamber which will be surrounded by coils used for magnetic field control. In the current experiment the coils are supplied with a maximum of 6 A [36]. The high current causes the coils to heat up and therefore also heat up the surrounding air. The following measurements are done in order to test the effect of this heating on the phase stability of the superlattice.
The first measurement is done while the coil is supplied with a current of 1.1 A. Before starting the measurement the setup had proper time to thermalize. It can thus be assumed that the effect of the heating caused by the coil is the only factor causing the changes in temperature. Figure 3.12 shows the comparison between the experimental data and the prediction using the modified Edlén equation and the recorded environmental data. During the measurement and because of the heating caused by the coil the temperature steadily increases during the measurement while both the pressure and the humidity only changed slightly. The effects of thermal expansion can therefore no longer be neglected compared to the change in relative phase as a result of the changes in refractive index. This is confirmed by the fact that the calculations using the Edlén equation can no longer reproduce the experimental data. Figure 3.13 shows that while the change of the measured relative phase dependent on the change in temperature (a) and that the calculations using the modified Edlén equation are mostly impacted by the change in pressure (c) rather than the change in temperature (b). During this measurement the main factor contributing to the phase change is no longer the change of the optical path distance caused by a change in refractive index[16] but rather a change in spatial path distance caused by thermal expansion. This effect is exaggerated because the setup these tests are conducted with is build without any optimization regarding thermal stability and utilizes standard optical components. To determine the effect the heating has on the phase φ of the individual lattices and the relative phase Θ between the two lattices, both are measured for different for different coil currents. Figure 3.14 shows a measurement of the relative phase Θ while the coil is heating up the setup. During the measurement the coil is supplied with a current of 2 A. After about 20 min the heating stats to slow down, indicating that the coil reached thermal equilibrium with the setup. For larger coil currents this is an issue because the box is not sealed air tight. Because of this the temperature inside the box cannot be increased by more than a few degree Celsius above the temperature inside the lab (even though the temperature of the coil is considerably higher). To get accurate values for the changes in temperature, phase and relative phase, only the first part of the measurement is considered for the least-square-fit (marked by the black dotted line in fig. 3.14). The resulting phase change $\Delta\varphi$, relative phase change $\Delta\Theta$ and temperature change ΔT for the currents are shown in figure 3.15. Because the relation between current and heating is different depending on the setup, $\Delta\varphi$ and $\Delta\Theta$ are depicted as a function

[16] As is the case in the ideal case where the change in pressure is large compared to the change in temperature.

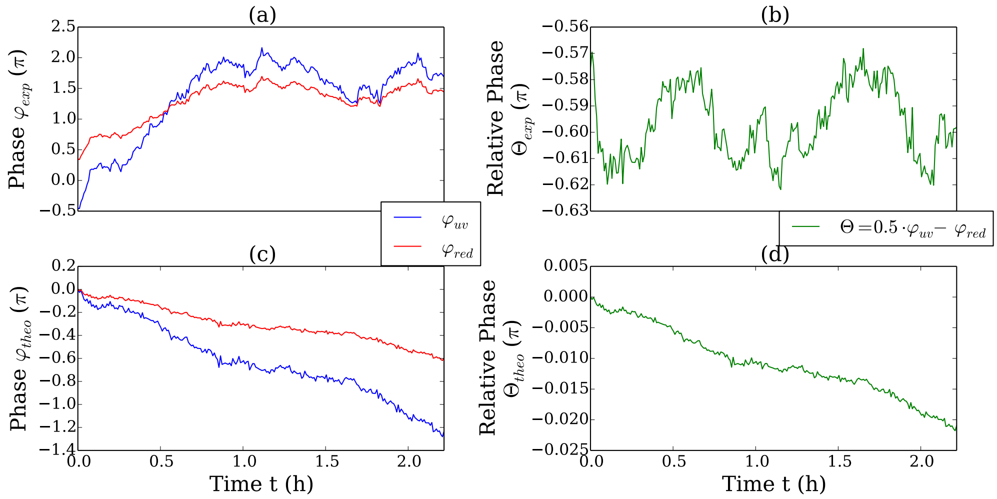

Fig. 3.12: Comparison between the experimental data (a) and (b) and the theoretical prediction using the modified Edlén equation (c) and (d).During the measurement the coil is supplied with a current of 1.1 A. The interval between two data points is approx. 20 s.

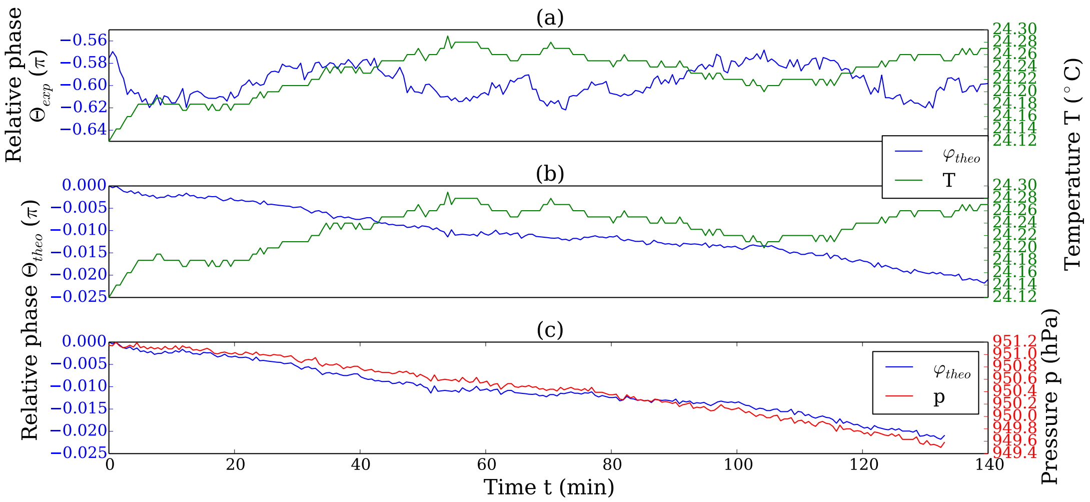

Fig. 3.13: Dependency between measured relative phase and temperature (a) and dependency of the calculated relative phase using the Edlén eqn. (b) and (c), corresponding to the measurement depicted in figure 3.12.

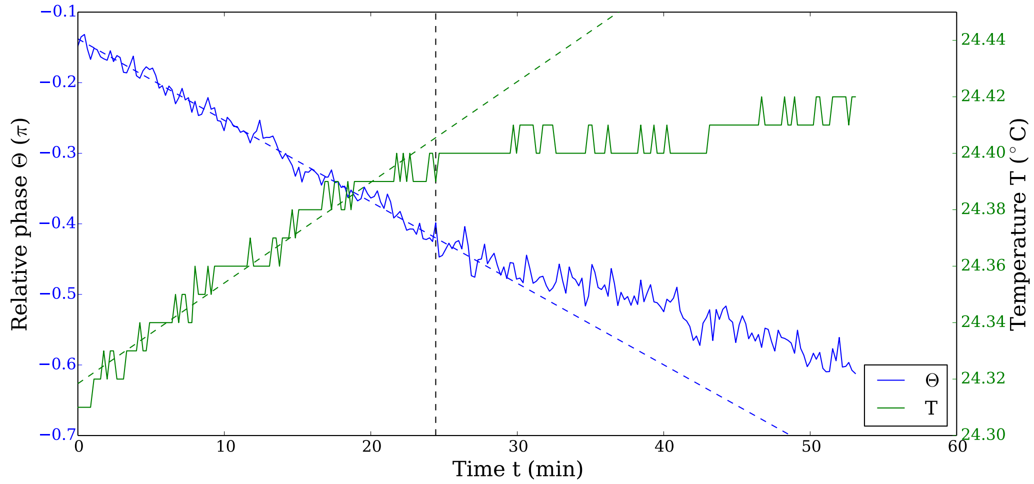

Fig. 3.14: Comparison between the relative phase of superlattice and the change in temperature. During the measurement the coil is supplied with a current of 2 A. The dotted lines indicate the linear regression functions used to calculate the relative phase change and temperature change, respectively. For the least-square-fit only data points up to and including the black dotted line are considered.

of temperature change ΔT in figure 3.16. For increasing temperature changes both the absolute amount of the phase change per hour as well as the absolute amount relative phase change per hour increase. For large changes in temperature, the relative phase changes on a scale that would severely hinder the experimental setup. As discussed before, the effect that the thermal expansion has on the change of both the phase and relative phase of the superlattice is far greater than the change caused by the change in the refractive index.

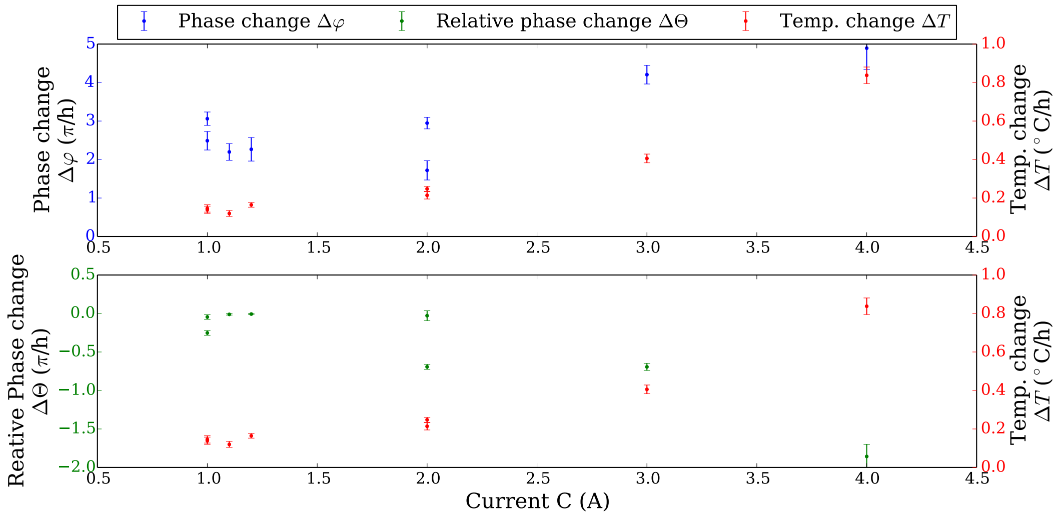

Fig. 3.15: Phase change $\Delta\varphi$ and relative phase change $\Delta\Theta$ both in units of π/h and temperature change ΔT in units of $^\circ C/h$ for different coil currents.

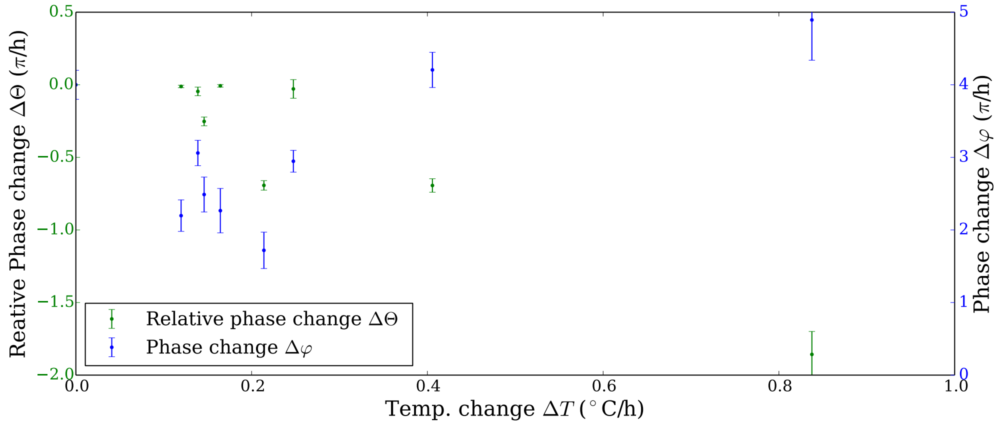

Fig. 3.16: Phase change $\Delta\varphi$ and relative phase change $\Delta\Theta$ as a function of temperature change ΔT.

4. Relative Phase Control

The measurements done previously show that the relative phase of the superlattice changes because of environmental changes (temperature, pressure and relative humidity) and thermal expansion of optical components. As even slight shifts in relative phase of the individual lattices can impact the geometry of the superlattice potential the relative phase has to be stabilized. One way the relative phase can be stabilized is by retroreflecting the red and the ultraviolet light on different mirrors. By mounting one of the mirrors on a positioning stage one of the spatial path distances of the light can be adjusted separately. In [4] it is stated that a long-term phase stability on the order of $1 \cdot 10^{-3}\,\pi$ is good enough for reliable experiments. In order to achieve this order of stability would mean that the spatial path distance has to be controlled on a sub-nanometer length scale. Because mechanical positioning stages cannot reach this high degree of precision a piezo-actuated positioning stage (piezo-stage) is used. These stages allow for theoretical resolutions of 0.76 nm and thus are sufficiently accurate. The following measurements act as a proof of concept that the relative phase can be controlled using such a setup. This is the first step of realizing an active stabilization of the relative phase of the superlattice.

4.1. Modified Experimental Setup

The experimental setup is modified by a second dichroic mirror (DCM) in order separate the two wavelengths and retroreflect them on different mirrors. The red light is reflected on a solid mounted mirror (M5.1) while the ultraviolet light is reflected on a movable mirror (M5.2) which is mounted on a piezo stage (Thorlabs: NF15AP25). The piezo-stage is driven using a piezo controller/High Voltage amplifier (Thorlabs: KPZ101) and is controlled via an external analog signal source using the SMA input of the piezo Controller. A schematic drawing showing just the modified part of the setup is depicted in figure 4.1. Because the two beams are now retroreflected on different mirrors the alignment of the setup gets more difficult. As established in equation (2.15), the spacing of the individual lattices is dependent on the angle between the mirrors in the two arms of the interferometer. To simulate the optical superlattice the spacing of the long lattice has to be twice that of the short lattice. This is achieved by first blocking the red light and adjusting only the mirrors used for the ultraviolet (M4, M5.2 and DCM) until vertical interference fringes are visible on the camera. Afterwards the ultraviolet light is blocked and using only the red light, mirrors M4 and M5.1 are adjusted until there are vertical interference fringes visible. Alignment is complete when both the red and the ultraviolet light produce vertical interference fringes and the spacing of the fringes caused by the red light is twice that the spacing caused by the ultraviolet light.

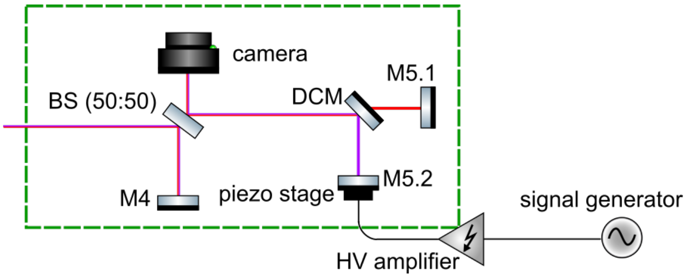

Fig. 4.1: The working part of the modified Michelson interferometer setup with the added second dichroic mirror and piezo-actuated stage. The rest of the setup stays as is depicted in figure 3.3. The mirrors used are M4 (Thorlabs: PF10-03-P01), M5.1 (Thorlabs: BB1-E02), M5.2 (Lens-Optics: M365/1"/45) and DCM (Thorlabs: DMLP-425).

4.1.1. Piezo-actuated positioning Stage

In order to successfully control the phase of the lattice the spatial path distance has to be changed on a nanometer length scale. This can be achieved using piezo-actuated positioning stages. The one used in this thesis is the NF15AP25 NanoFlex single-axis flexure stage from Thorlabs. This positioning stage offers a theoretical resolution of 0.76 nm with 25 µm travel [37]. It is driven with the KPZ101 K-Cube piezo controller from Thorlabs. This controller allows operating bandwidths up to 1 kHz [38]. The piezo stage can be supplied with a 0 V to 75 V voltage. The input voltage range of the piezo controller is 0 V to 10 V, where an input voltage of 10 V corresponds to an output voltage of 75 V. Assuming that the maximum travel of the stage is 25 µm, the travel of the stage can be expressed as a function of input voltage U_{in} at the controller leading to:

$$x_{\mathrm{travel}}(U_{\mathrm{in}}) = \frac{25\,\mu\mathrm{m}}{10\,\mathrm{V}} \cdot U_{\mathrm{in}} = 2.5\,\mathrm{nm/mV} \cdot U_{\mathrm{in}} \tag{4.1}$$

4.2. Results

The piezo-stage is modulated with a low frequency sine wave using a signal generator [17]. This modulates the phase of the interference fringes of the ultraviolet light. Therefore the relative phase changes accordingly. Figure 4.2 shows a measurement done with a modulation frequency of $f_{\mathrm{mod}} = 5\,\mathrm{mHz}$ and a peak-to-peak amplitude of $V_{pp} = 10\,\mathrm{mV}$. In subfigure 4.2(b) the pure sine modulation of φ_{uv} gets additionally shifted as a result of the phase change due to changes in refractive index and thermal expansion of the setup. In subfigure 4.2(c) the waveform of the modulation becomes more visible. The relative phase is calculated using both the phase of the red and the ultraviolet lattice. Because of this, global changes that affect both the red and the ultraviolet light, for example due to thermal expansion cancel each other.
In order to calculate the amplitude of the phase change, first the travel of the piezo-stage

[17]Model used: Keithley 3390

Tab. 4.1: Fit parameters given by the least-square fits (equation (4.4)) of the phase φ and relative phase Θ for a measurement where the piezo-stage was modulated using a sine wave with a peak-to-peak modulation amplitude of $A_{pp} = 10\,\mathrm{mV}$ and a modulation frequency of $f_{\mathrm{mod}} = 5\,\mathrm{mHz}$. The corresponding measurement and fits are shown in figure 4.2.

	a ($\pi/10^{-3}$)	δ (π)	A (π)	f (mHz)	φ (π)
$f_{\varphi_{\mathrm{uv}}}$	0.5960(413)	−0.4630(149)	0.1240(336)	4.9500(742)	2.508(171)
f_Θ	−0.088 90(142)	−0.453 00(231)	0.058 00(519)	5.0020(255)	−1.3150(569)

is calculated using equation (4.1):

$$x_{\mathrm{travel}} = 2.5\,\mathrm{nm/mV} \cdot 10\,\mathrm{mV} = 25\,\mathrm{nm} \tag{4.2}$$

Because the light gets retroreflected on the mirror, the spatial path the light has to propagate is twice the travel distance of the piezo-stage. The peak-to-peak amplitude of the phase change can then be calculated:

$$A_{pp} = \frac{2\pi}{362\,\mathrm{nm}} \cdot 2 \cdot 25\,\mathrm{nm} = 0.8678 = 0.2762\pi \tag{4.3}$$

In subfigure 4.2(b) a least-square curve fitting method is used to fit a function $f_{\varphi_{\mathrm{uv}}}(t)$ to the data points measured for φ_{uv}, that includes a superposition of a linear offset and a sinusoidal modulation:

$$f(t) = \underbrace{a \cdot t + \delta}_{\text{offset}} + \underbrace{A \sin(2\pi \cdot f \cdot t + \varphi)}_{\text{modulation}} \tag{4.4}$$

In subfigure 4.2(c) the same curve fitting method is used again to fit a function $f_\Theta(t)$ to the data points calculated for Θ using the same function. The fit parameters are calculated using a least-square-fit and are listed in table 4.1. The fit parameter translate to a peak-to-peak modulation amplitude of $A_{pp} = 0.2480(672)\pi$ and a modulation frequency of $f_{\mathrm{mod}} = 4.950(74)\,\mathrm{mHz}$ for the modulation of φ_{uv} and a peak-to-peak modulation amplitude of $A_{pp} = 0.116\,00(1038)$ and a modulation frequency of $f_{\mathrm{mod}} = 5.0020(255)\,\mathrm{mHz}$ for Θ. The modulation amplitude of the relative phase Θ is expected to be half that of the phase of the lattice created by the ultraviolet light φ_{uv} because $\Theta = 0.5 \cdot \varphi_{\mathrm{uv}} - \varphi_{\mathrm{red}}$. The measurement shows that both the phase of the individual interference patterns (in this case φ_{uv}) and the relative phase Θ can be modulated using a piezo-actuated positioning stage. This is the first step of actively controlling the phase/relative phase of the superlattice. Using this setup an appropriate error-signal can be used to control the piezo-stage resulting in an active feedback loop [39]. Using the camera to extract the phase information limits the expected bandwidth of the active stabilization to the exposure time of the camera. With the current setup the smallest interval between two images is on the order of seconds [18]. Which is the reason why the piezo-stage is

[18] Which is not only due to the exposure time of the camera but rather due to the time it takes to collect the data from the environmental sensor.

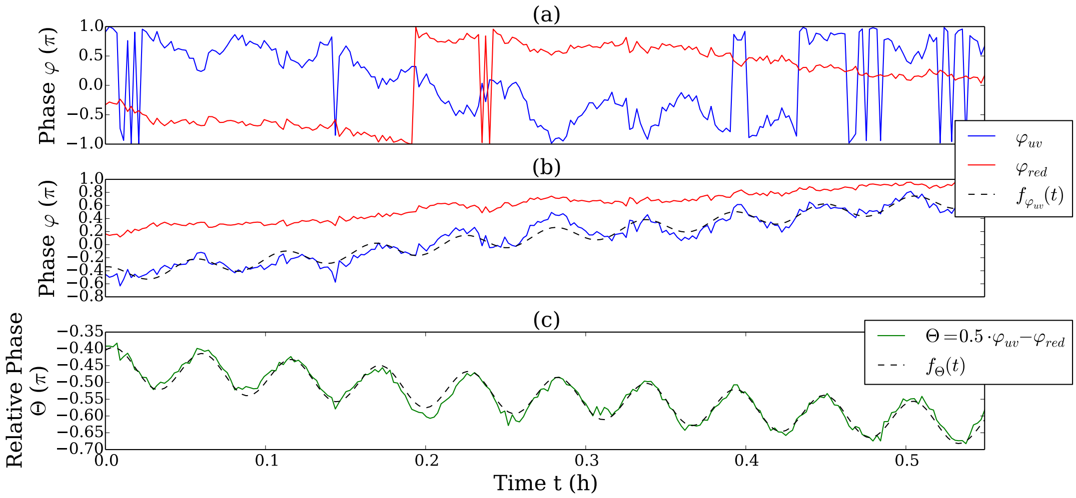

Fig. 4.2: During this measurement the position of he piezo-stage was modulated using a sine wave with a peak-to-peak modulation amplitude of $A_{pp} = 10\,\mathrm{mV}$ and a modulation frequency of $f_{\mathrm{mod}} = 5\,\mathrm{mHz}$. Subfigure (a) shows the measured phase data of both wavelengths, subfigure (b) shows the adjusted data and (c) shows the relative phase Θ. The two black curves correspond to two functions fitted to the experimental data.

modulated using the low frequency sine wave. The evaluation of the images using the Fourier transform method also has to be taken into account. For example in [39] the author states that by using a Raspberry Pi and a Pi NoIR Camera the setup can only handle between 1.5 and 4 phase measurements per second. For slow fluctuations of the relative phase, caused for example by environmental changes, this is low bandwidth is sufficient as the environmental changes causing the phase shifts take place on a time scale of minutes. However in order to actively tune the relative phase for experiments or stabilize faster fluctuations the bandwidth of the stabilization has to be increased.
The measurements done with the modulated piezo-stage also serve as a confirmation that the method used to extract the phase information is correct. Both the measured peak-to-peak modulation amplitude and the modulation frequency agree quite well with the values set at the signal generator.

5. Conclusion and Outlook

The main task of this thesis was to test the phase stability of the superlattice setup in regard of changing environmental conditions. To test the stability a two wavelength Michelson interferometer setup was used in order to superimpose two one-dimensional optical lattices. The phase of the individual lattices was determined by performing a discrete Fourier transform of the image data. The refractive index was calculated using the modified Edlén equation which is an empirical formula that takes into account the ambient temperature, pressure and relative humidity in order to calculate the refractive index of air. Of the three environmental factors considered for the calculation of the refractive index, the air pressure has the biggest effect on the phase. It is also the only factor that cannot be easily controlled in our laboratory environment. While the ambient pressure is expected to change on a time scale of hours, the air pressure can also change locally as a result of air flow suggesting that the superlattice setup should be enclosed or shielded in order to protect it against such rapid and unpredictable changes in air pressure.
The measurements show that the phase change caused by a change of the refractive index can be reliably predicted using the calculations with the modified Edlén equation. However for large temperature fluctuations the effect of thermal expansion exceeds the effect of the dispersion and the calculations using the modified Edlén equation failed to predict the phase change. In the new experiment the superlattice will be located near coils which are used for the magnetic field control of the experiment. These coils heat up the surrounding air while operating. By solid mounting the components on materials with low thermal expansion coefficients or by using monolithic mounts the effect of the thermal expansion can be reduced [40]. It is also possible to reduce the heating by water cooling the coils [41]. It was determined that for the two wavelengths used in the superlattice setup the phase change as a result of environmental changes, under optimal conditions and without additional heating, can be on the order of $0.5\,\pi$ per hour and that the relative phase change can be on the order of $0.05\,\pi$ per hour. This means that the long-term stability of the superlattice is not good enough and that external stabilization is required. As even small shift in relative phase on the order of $0.01\,\pi$ can result in potential shifts that would make reliable and repeatable experiments impossible. By performing phase centering measurements in regular intervals the long-term stability can be improved [4]. The experiment takes place on a time scale of minutes per cycle. On small time scales the relative phase exhibits changes on the order of $0.005\,\pi$ due to for example the previously mentioned air flow. Achieving a better phase stability can be done passively by reducing the effect of environmental changes. This is possible by enclosing the beam path in sealed glass tubes [32] or reducing the path length [18]. As a first step of realizing an active stabilization of the relative phase the setup was changed such that it allowed the two beams to be retroreflected on separate mirrors. One of the mirrors was mounted onto a piezo-actuated positioning stage. This allowed the relative phase of the superlattice to be actively changed by shifting the position of the piezo-stage. By utilizing an appropriate error signal to control the position of the piezo-stage this setup could be used to actively stabilize the relative phase.

This thesis laid down the requirements for a stable optical supperlattice setup. It has to be experimentally tested what the requirements for the long-term phase stability are in order to achieve reliable experimental conditions for the optical superlattice and what methods of phase stabilization can be included into the new experimental setup.

List of Figures

A. Laser setup

A schematic drawing of the laser setup is depicted in figure A.1. The system is controlled via Ethernet and the SolsTis Control page. The wavelength can be set on the control page. There are separate locks ensuring a stable output, the SolsTis „Etalon-lock“ and the ECD-X module „Cavity-lock“ . Both can be controlled automatically via the control page. When starting up the system, after ramping up the power of the pump laser, the system has to be aligned which is also done automatically by using the *One Shot* alignment function on the control page. The output of the ultraviolet light can as high as 1.4 W at a wavelength of 362 nm, while the output of the red light (724 nm) at the variable pick off is at least 0.4 W. The split between the pick-off and the ECD-X module can be adjusted by rotating $\lambda/2$-waveplate located between the SolsTis Laser Head and the variable IR pick-off.

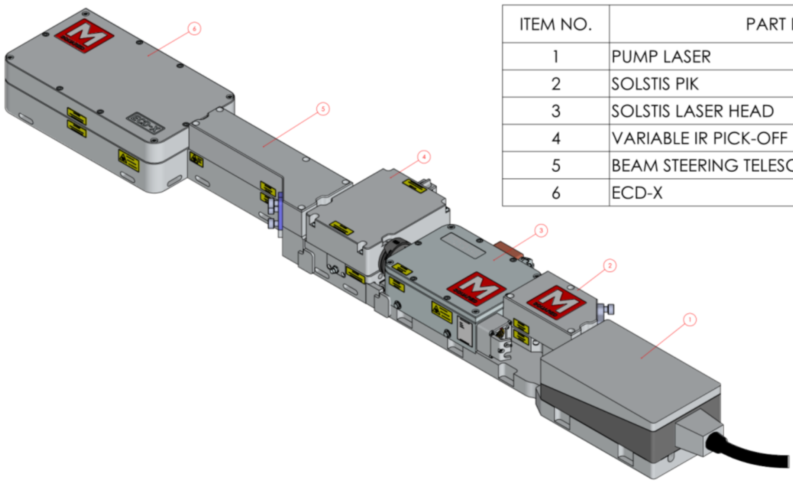

ITEM NO.	PART DESCRIPTION
1	PUMP LASER
2	SOLSTIS PIK
3	SOLSTIS LASER HEAD
4	VARIABLE IR PICK-OFF
5	BEAM STEERING TELESCOPE
6	ECD-X

Fig. A.1: Schematic drawing of the laser setup used to create the two wavelengths used during the experiment [42].

B. Modified Edlén equation

The modified Edlén equation used to calculate the refractive index of air is an empirical formula published by G. Bönsch et. al in 1998 [24]. Because of its empirical nature many constants go into the calculation. The calculations of the refractive index using the modified Edlén equation are summarized hereinafter and follow the ones done in [43].

```python
"""
    calculating the refractive index using the
    modified edlen equation
"""

def svp_water(t):
    """
        Saturation vapour pressure over water at given temperature.

        inputs:
        t :
        Air temperature in degree Celsius.

        Returns:
        p_sv :
        Saturation vapour pressure of water, at the given
        temperature, in Pascal.
    """

    K1 = 1.16705214528e+03
    K2 = -7.24213167032e+05
    K3 = -1.70738469401e+01
    K4 = 1.20208247025e+04
    K5 = -3.23255503223e+06
    K6 = 1.49151086135e+01
    K7 = -4.82326573616e+03
    K8 = 4.05113405421e+05
    K9 = -2.38555575678e-01
    K10 = 6.50175348448e+02

    T = t + 273.15 # convert degree celsius to kelvin

    omega = T + K9 / (T - K10)
    A = omega ** 2 + K1 * omega + K2
    B = K3 * omega ** 2 + K4 * omega + K5
    C = K6 * omega ** 2 + K7 * omega + K8
    X = -B + math.sqrt(B ** 2 - 4 * A * C)

    p_sv = 1.0e6 * ((2.0 * C / X) ** 4)

    return p_sv
```

```python
def edlen_equation(_lambda, t, p, rh):
    """
        Refractive index of air according to the Edlen equation.

        inputs:
        _lambda :
        Wavelength in vacuum, in nano-meters. Valid wavelength range
        is 300nm - 1700nm.
        t :
        Temperature in degree Celsius. Valid temperate range is
        -40 to 100 degree Celsius.
        p :
        Pressure in Pascal. Valid range is from 10kPa - 140 kPa.
        rh :
        Relative humidity in [0 - 100].

    """

    A = 8342.54
    B = 2406147
    C = 15998
    D = 96095.43
    E = 0.601
    F = 0.00972
    G = 0.003661

    _lambda = _lambda * 1.0e-3
    T = t + 273.15 # convert degree celsius to kelvin

    S = 1.0 / _lambda ** 2
    ns = 1 + 1e-8 * (A + B / (130.0 - S) + C / (38.9 - S))
    X = (1 + 1e-8 * (E - F * t) * p) / (1 + G * t)
    ntp = 1 + p * (ns - 1) * X / D

    # Convert relative humidity to water vapour partial pressure
    pv = (rh / 100.0) * svp_water(t)

    n = ntp - 1e-10 * ((292.75 / T) * (3.7345 - 0.0401 * S)) * pv

    return n
```

References

[1] Immanuel Bloch. Ultracold quantum gases in optical lattices. *Nature Physics*, 1(1):23–30, Oct 2005.

[2] +W.+S. Bakr, +A. Peng, +M.+E. Tai, +R. Ma, +J. Simon, +J.+I. Gillen, +S. Fölling, +L. Pollet, and +M. Greiner. Probing the superfluid–to–mott insulator transition at the single-atom level. *Science*, 329(5991):547–550, 2010.

[3] Markus Greiner, Olaf Mandel, Tilman Esslinger, Theodor W. Hänsch, and Immanuel Bloch. Quantum phase transition from a superfluid to a mott insulator in a gas of ultracold atoms. *Nature*, 415(6867):39–44, Jan 2002.

[4] Michael Lohse. *Topological charge pumping with ultracold bosonic atoms in optical superlattices*. PhD thesis, Ludwig Maximilian Univerity of Munich, 2018.

[5] T. H. MAIMAN. Stimulated optical radiation in ruby. *Nature*, 187(4736):493–494, 1960.

[6] Harald Friedrich. *Theoretical Atomic Physics*. Springer International Publishing, 2017.

[7] Albert Einstein. Quantentheorie des einatomigen idealen gases. 1924.

[8] Bose-einstein condensate: A new form of matter, Oct 2001.

[9] Axel Griesmaier, Jörg Werner, Sven Hensler, Jürgen Stuhler, and Tilman Pfau. Bose-einstein condensation of chromium. *Physical Review Letters*, 94(16), Apr 2005.

[10] J. Stuhler. Observation of dipole-dipole interaction in a degenerate quantum gas. *Physical Review Letters*, 95(15), 2005.

[11] Igor Ferrier-Barbut. Observation of quantum droplets in a strongly dipolar bose gas. *Physical Review Letters*, 116(21), 2016.

[12] Matthias Schmitt, Matthias Wenzel, Fabian Böttcher, Igor Ferrier-Barbut, and Tilman Pfau. Self-bound droplets of a dilute magnetic quantum liquid. *Nature*, 539(7628):259–262, Nov 2016.

[13] Matthias Wenzel, Fabian Böttcher, Jan-Niklas Schmidt, Michael Eisenmann, Tim Langen, Tilman Pfau, and Igor Ferrier-Barbut. Anisotropic superfluid behavior of a dipolar bose-einstein condensate. *Physical Review Letters*, 121(3), 2018.

[14] Luca Tanzi, Eleonora Lucioni, Francesca Famà, Jacopo Catani, Andrea Fioretti, Carlo Gabbanini, and Giovanni Modugno. Observation of stable stripes in a dipolar quantum gas. *submitted, arXiv: 1811.02613*, 11 2018.

[15] Fabian Böttcher, Jan-Niklas Schmidt, Matthias Wenzel, Jens Hertkorn, Mingyang Guo, Tim Langen, and Tilman Pfau. Transient supersolid properties in an array of dipolar quantum droplets. *submitted, arXiv: 1901.07982*, 01 2019.

[16] A quantum gas microscope for highly dipolar atoms, Apr. 2017.

[17] Robert Roth and Keith Burnett. Ultracold bosonic atoms in two-colour superlattices. *Journal of Optics B: Quantum and Semiclassical Optics*, 5(2):S50–S54, Apr 2003.

[18] Christian Neustetter. Building a superlattice for ultracold ^{87}Rb-atoms. Master's thesis, University of Innsbruck, 2007.

[19] D. Meschede. *Optik, Licht und Laser*. B. G. Teubner, 1. edition, 1999.

[20] Wolfgang Demtröder. *Experimentalphysik II*. Springer Spektrum, 6. edition, 2013.

[21] Eugene Hecht. *Optik*. Oldenbourg, 2. edition, 1999.

[22] Torsten Fließbach. *Elektrodynamik*. Springer Spektrum, 6. edition, 2012.

[23] Bengt Edlén. The refractive index of air. *Metrologia*, 2(2):71–80, Apr 1966.

[24] G Bönsch and E Potulski. Measurement of the refractive index of air and comparison with modified edl n's formulae. *Metrologia*, 35(2):133–139, Apr 1998.

[25] Liping Yan, Benyong Chen, Enzheng Zhang, Shihua Zhang, and Ye Yang. Precision measurement of refractive index of air based on laser synthetic wavelength interferometry with edlén equation estimation. *Review of Scientific Instruments*, 86(8):085111, Aug 2015.

[26] T. C. Li, H. Kelkar, D. Medellin, and M. G. Raizen. Real-time control of the periodicity of a standing wave: an optical accordion. *Optics Express*, 16(8):5465, Apr 2008.

[27] Thomas Uehlinger. Artificial graphene with tunable interactions. *Physical Review Letters*, 111(18), 2013.

[28] Florian Huber. *Site-resolved imaging with the fermi gas microscope*. PhD thesis, Harvard University, 2014.

[29] Rikesh Patel, Samuel Achamfuo-Yeboah, Roger Light, and Matt Clark. Widefield two laser interferometry. *Optics Express*, 22(22):27094, Oct 2014.

[30] Su-Heng Zhang. Spatial interference: From coherent to incoherent. *Physical Review Letters*, 102(7), 2009.

[31] Michael E. Zucker. Ligo precision understated. *Physics Today*, 60(5):16–16, May 2007.

[32] Xiao-Fan Xu. *Manipulating quantum entanglement with atomic ensembles and with atoms in optical superlattices*. PhD thesis, Rupert-Carola University of Heidelberg, 2014.

[33] Thorlabs. *Product documentation BSW10*.

[34] James W. Cooley and John W. Tukey. An algorithm for the machine calculation of complex fourier series. *Mathematics of Computation*, 19(90):297–297, May 1965.

[35] SciPy.org. Numpy v1.13 manual - discrete fourier tranform.

[36] Holger Kadau. *Rosensweig Instability and Droplets in a Qantum Ferrofluid of Dysprosium Atoms*. PhD thesis, University of Stuttgart, 2016.

[37] Thorlabs. *NF15AP25 1.5 mm Travel Single Axis Flexure Stages, User Guide - Rev. G*, Oct 2018.

[38] Thorlabs. *KPZ101 Piezo Driver, Kinesis User Guide - Rev. Dk*, Jan 2017.

[39] Carolin Dietrich. An accordion-type lattice: A tuneable dipole trap for ultracold gases. Master's thesis, University of Stuttgart, 2018.

[40] Luca Schmitt. Setting up an optical accordion lattice, 2018.

[41] Thomas Maier. *Interactions in a Qunatum Gas of Dysprosium Atoms*. PhD thesis, University of Stuttgart, 2015.

[42] M Squared Lasers Ltd. *ECD-X Quick Reference Guide V1.1*.

[43] NIST. Index of refraction of air.

[44] The optical component library was provided by: Alexander Franzen. Componentlibrary, creative commons attribution-noncommercial 3.0 unported license. 2009.

Danksagung

An dieser Stelle möchte ich mich bei all den Leuten bedanken, die zum Gelingen dieser Bachelorarbeit beigetragen haben.

Zunächst möchte ich mich bei Prof. Dr. Tilman Pfau dafür bedanken, dass ich im Rahmen dieser Bachelorarbeit an der aktiven Forschung des 5. Physikalischen Instituts teilhaben durfte. Außerdem möchte ich mich für durchweg positive Atmosphäre und die vielen Aktivitäten des Instituts bedanken.

Bei den Dysis, die mich herzlich in ihrem Team aufgenommen haben und mir tiefe Einblicke in ihre aktuelle Forschungsarbeit ermöglicht haben. Gerade in dieser sehr spannenden Zeit voller neuen experimentellen Ergebnissen wurde mir gezeigt wie Problemstellungen in einem physikalischen Labor gelöst werden und was es heißt Forschung zu betreiben.
Vor allem möchte ich mich hier bei Jan-Nicklas Schmidt für die Betreuung meiner Arbeit und die Hilfe bei der Lösung von technischen und theoretischen Problemen und bei Fabian Böttcher für die Hilfe bei optischen Aufbauten bedanken.

Allen Mitarbeiterinnen und Mitarbeitern des 5. Physikalischen Instituts der Universität Stuttgart, für die gesprächigen Kaffeerunden und die lehrreichen Breakfast Talks.

Bei Matthias Schmidt und Felix Kogel, die maßgeblich an dem Erfolg meines Studiums beteiligt waren.

Bei meiner Mutter für die finanzielle und ideelle Unterstützung meines Studiums.